

1 Quantifying Temperature-sliding Inconsistency in Thermomechanical Coupling: A
2 Comparative Analysis of Geothermal Heat Flux Datasets at Totten Glacier

3
4 Junshun Wang¹, Liyun Zhao¹, Michael Wolovick^{2,3}, John C. Moore³ Moore⁴

5 ¹State Key Laboratory of Earth Surface Processes and Hazards Risk Governance
6 (ESPHR), Faculty of Geographical Science, Beijing Normal University, Beijing
7 100875, China

8 ²[Glaciology](#)²[Center for Industrial Mathematics \(ZeTeM\)](#), University of Bremen,
9 Bremen, Germany

10 ³[Glaciology](#) Section, Alfred-Wegener-Institut, Helmholtz-Zentrum für Polar- und
11 Meeresforschung, Bremerhaven, Germany

12 ³[Arctic](#)⁴[Arctic](#) Centre, University of Lapland, Rovaniemi, Finland

13 *Correspondence:* Liyun Zhao (zhaoliyun@bnu.edu.cn), John C. Moore
14 (john.moore.bnu@gmail.com)

15
16
17
18 **Abstract.** Rapid sliding of ice sheets requires warm basal temperatures and lubricating
19 basal meltwater, whereas slow velocities typically correlate with a frozen bed. However,
20 ice sheet models often infer basal sliding by inverting surface velocity observations
21 with the vertical structure of temperature and hence rheology held constant. If the
22 inversion is allowed to freely vary sliding over the model domain, then inconsistencies
23 between the basal thermal state and ice motion can arise lowering simulation realism.
24 In this study, we propose a new method that quantifies inconsistencies when inferring
25 thawed and frozen-bedded regions of ice sheets. This method can be used to evaluate
26 the quality of ice sheet simulation results without requiring any englacial or subglacial
27 measurements. We apply the method to evaluate simulation results for Totten Glacier
28 using an isotropic 3D full-Stokes ice sheet model with eight geothermal heat flux (GHF)
29 datasets and compare our evaluation results with inferences on basal thermal state from
30 radar specularity. The rankings of GHF datasets based on inconsistency are closely
31 aligned with those using the independent specularity content data. Examples of the
32 method utility are 1. an overcooling inconsistency with all GHFs near the western
33 boundary of Totten Glacier between 70°S-72°S, where there is a bedrock canyon and
34 fast surface ice velocities, suggesting that all GHFs are low; 2. an overheating
35 inconsistency in the eastern Totten Glacier with all GHFs suggesting overestimation of
36 ice temperature due, in this case, to ~~an unrealistically~~ a warm bias in the surface

37 temperature. Our approach opens a new avenue for assessing the self-consistency and
38 reliability of ice sheet model results and GHF datasets, which may be widely applicable.

39 40 1. Introduction

41 Ice sheet models are an important tool for projections of ice sheet mass balance
42 and their contribution to sea level rise. Ice sheet models are usually initialized by “spin-
43 up” or data assimilation such that they reproduce the present-day geometry or surface
44 velocity of an ice sheet (Seroussi et al., 2019). Often ice sheet model simulations derive
45 ice dynamics using ice temperatures taken from other studies (e.g., Gillet-Chaulet et al.,
46 2012; ~~Van Liefferinge and Pattyn, 2013~~; Cornford et al., 2015; Pittard et al., 2016;
47 Siahaan et al., 2022). In thermo-mechanically coupled ice sheet simulations, the ice
48 sheet model is usually spun up with idealized temperature-depth profiles and then run
49 in a thermo-mechanically coupled mode constrained by geothermal heat flux (GHF)
50 and surface ice temperature fields (Seroussi et al., 2019). While advances in satellite
51 and field observation technologies have led to a preliminary consensus on ice sheet
52 geometry and surface ice temperature, significant uncertainties persist in basal
53 boundary conditions, including GHF and basal friction, since reliable observational
54 data are scarce. These basal properties introduce significant uncertainty in the simulated
55 ice sheet dynamics, and thus ice sheet mass balance.

56 The GHF, the heat flow from the Earth's crust to the base of ice sheet, is a critical
57 variable in the basal boundary condition for simulating the ice temperature profile, and
58 hence ice rheology and flow dynamics (Fisher et al., 2015; Smith - Johnsen et al., 2020;
59 Reading et al., 2022). Several GHF datasets exist, derived in various ways from
60 geophysical observations and models, and they exhibit significant variability in both
61 spatial distribution and magnitude (e.g., An et al., 2015; Dziadek et al., 2017; Martos et
62 al., 2017; Shen et al., 2020; Stål et al., 2021). These GHF datasets have been widely
63 used in thermodynamic simulations of Antarctica (e.g., McCormack et al., 2022;
64 Shackleton et al., 2023; Park et al., 2024; Van Liefferinge et al., 2018). However,
65 assessing the GHF field accuracy is problematic because in situ measurements such as
66 boreholes are sparse. Few studies have assessed the quality and reliability of GHF
67 datasets over specific regions. Kang et al. (2022) employed a combination of forward
68 model and inversion using a 3D full-Stokes ice flow model to simulate the basal thermal
69 state in the Lambert–Amery Glacier region and evaluate different GHFs using the
70 locations of subglacial lakes, but the constraints used were asymmetric between frozen
71 and thawed beds, and assigned inflated reliability to the warmer GHF maps. Indirect
72 estimates of basal conditions have used airborne radar specularity content (Schroeder
73 et al., 2013, 2015; Young et al., 2016) as proxies for basal wetness/dryness and thermal
74 regime (Dow et al., 2020). Huang et al. (2024) used an inverse modeling approach
75 similar to that of Kang et al. (2022) for Totten Glacier and combined this with measured

76 radar specularity content to derive a two-sided constraint on the basal thermal state in
77 addition to subglacial lakes locations. However, specularity content is not yet available
78 for many regions of Antarctica.

79 The basal friction field is another poorly known boundary condition in ice sheet
80 modeling, and a key source of uncertainty in the long-term projection of ice sheets and
81 glaciers. Although basal slip is crucial to the 3D ice flow, it is difficult to observe.
82 Several basal sliding parameterizations have been proposed and widely used
83 (Weertman, 1957; Kamb, 1970; Nye, 1970; Budd et al., 1979; Fowler, 1981; Schoof,
84 2005; Gagliardini et al., 2007; Gladstone et al., 2014; Tsai et al., 2015; Brondex et al.,
85 2017, 2019). The linear Weertman basal sliding parameterization is the most widely
86 used due to its simple form. Given prescribed or modelled ice temperatures and hence
87 ice viscosity, numerous studies have inferred the spatial distribution of the basal friction
88 coefficient over grounded ice to best match observed present-day surface ice velocities
89 or ice sheet geometry using snapshot or time-dependent data assimilation and inverse
90 methods (MacAyeal, 1993; ~~Morlighem et al., 2010; Rignot et al., 2011~~; Gillet-Chaulet
91 et al., 2012; Larour et al., 2012; Pollard and DeConto, 2012; Morlighem et al., 2013;
92 ~~Perego et al., 2014~~; Pattyn, 2017; Albrecht et al., 2020; Lipscomb et al., 2021; Choi et
93 al., 2023). However, such inversions typically allow the friction coefficient to vary
94 freely to match the surface velocity observations. This can potentially lead to conflicts
95 with the temperature field used during the inversion, ~~which we refer to as~~
96 ~~“inconsistencies” in this study.~~ For instance, relatively fast surface ice velocity may
97 demand basal sliding in areas where the basal temperatures are below the local pressure
98 melting point. ~~These inconsistencies may be due to unrealistic ice temperatures or a~~
99 ~~lack of complete physics in the ice sheet model.~~ However, many studies overlook this
100 aspect, and use the inversion results to initialize ice sheet dynamics simulations and
101 estimate glacier mass balance and its contribution to sea level rise (Seroussi et al., 2019;
102 Peyaud et al., 2020; Schannwell et al., 2020; Payne et al., 2021).

103 For this study, we define the inconsistencies as differences between a sliding
104 inversion and the temperature/rheology field used as an input to that inversion. More
105 specifically, the inconsistencies are between modelled basal sliding (which is tuned to
106 match the observed fast surface velocity during the inversion) and modelled frozen bed,
107 and between observed slow surface velocity (which is most likely indicative of a non-
108 slip basal condition) and modelled thawed bed. The inconsistencies originate from
109 multiple causes, including uncertainties in GHF, surface ice temperature, ice sheet
110 geometry, bed topography, surface velocity, ice density and incomplete ice flow
111 mechanics.

112 To the best of our knowledge, there has been no study of such inconsistencies
113 ~~between a sliding inversion and the temperature/rheology field used as an input to that~~
114 ~~inversion.~~ Here we develop a novel and generally applicable method to estimate this

115 inconsistency without relying on basal observation data. We utilize ~~the inconsistency~~
116 ~~of the modelled ice temperature and observed velocity field~~
117 ~~this approach~~ to evaluate
118 the quality of ice flow model results. Notably, this approach can also serve as a
119 supplementary method for assessing geothermal heat flux datasets, relying solely on
surface ice velocity observations rather than additional englacial or subglacial data.

120 We apply our method to Totten Glacier, a primary outlet of the Aurora subglacial
121 basin in East Antarctica (Greenbaum et al., 2015; Pritchard et al., 2009). The Totten
122 Glacier subregion experienced the largest mass loss among drainage basins in East
123 Antarctica during the period 1979-2017 and 2003-2020 (Kim et al., 2024; Rignot et al.,
124 2019) (Fig. 1a). We examine inconsistencies between simulated ice temperature and ice
125 velocity fields ~~from Huang et al. (2024)~~ using a 3D full-Stokes model ~~using with~~ the
126 various GHFs ~~included in Huang et al. (2024)~~, and ~~we~~ use this analysis to rank the
127 reliability of different GHF fields. This GHF ranking closely resembles that reported
128 by Huang et al. (2024), which used the agreement between the modelled basal thermal
129 regime and specularity content, which we take as a validation of the method. Since the
130 new method does not require any englacial or subglacial data, it can be applied to many
131 glaciers, particularly those lacking observations. Our approach can provide a swift
132 assessment of the plausibility of basal temperature and velocity simulated by ice sheet
133 models. Additionally, it can be effectively utilized to map the spatial distribution of
134 GHF over- or under-estimation.

135

136 **2. Method**

137 **2.1 Methodology in this study**

138 ~~The inconsistencies defined in this study are essentially~~ between a sliding inversion
139 and the temperature/rheology field used as an input to that inversion. More specifically, the
140 ~~inconsistencies are between modelled basal sliding (which is tuned to match the observed~~
141 ~~fast surface velocity during the inversion) and modelled frozen bed, and between observed~~
142 ~~slow surface velocity (which is most likely indicative of a non-slip basal condition) and~~
143 ~~modelled thawed bed. The inconsistencies originate from multiple causes, including~~
144 ~~uncertainties in GHF, surface ice temperature, ice sheet geometry, bed topography, surface~~
145 ~~velocity, ice density and incomplete ice flow mechanics.~~

146 **2.1.1 Definition of Metrics**

147 There is no direct correlation between basal temperature and surface velocity;
148 rather, they are linked through the basal thermal state - the basal temperature being at
149 or below the pressure melting point. The ice bottom in the study domain can be
150 partitioned into thawed and frozen beds depending on whether the simulated basal ice
151 temperature reaches the local pressure melting point. To effectively penalize models
152 exhibiting both localized overheating (bed too warm) and overcooling (bed too cold),
153 we establish overheating metrics within the thawed-bedded region and overcooling

154 metrics within the frozen-bedded region to quantitatively assess the inconsistency
155 between the simulated temperature and velocity fields. Thus, we provide two-sided
156 constraints on the temperature field that penalize both too high and too low ice
157 temperature.

158 Overcooling occurs where basal temperature is underestimated. Crucially, in
159 regions with relatively fast observed surface velocity, the inverse method nevertheless
160 yields a nonzero basal velocity — a physically inconsistent result given the cold basal
161 temperature. When basal ice temperature is below the pressure melting point, the basal
162 modelled velocity is expected to approach zero. This inconsistency is larger for faster
163 simulated basal ~~ice speedvelocity magnitude~~ and for colder simulated basal
164 temperatures. We therefore use a formula that accounts for both variables to quantify
165 overcooling:

$$AOC = (T_{melt} - T_{bm}) \times U_{bm}, \quad (1)$$

166 where AOC stands for absolute overcooling, T_{melt} is the basal pressure melting point,
167 T_{bm} represents the simulated basal ice temperature and U_{bm} means the simulated basal
168 ~~ice speedvelocity magnitude~~.

169 ~~For the overheating metric, since the first term of the right hand side of Eq. (1)
170 becomes zero at a thawed bed, we cannot use a similar formula as Eq. (1).~~ It is not
171 straightforward to quantify the inconsistencies between modelled thawed bed and
172 expected slow basal ~~speedvelocity magnitude~~ given slow observed surface
173 ~~speedvelocity magnitude~~. We note the fact that modelled basal sliding ~~speedvelocity~~
174 ~~magnitude~~ must remain non-negative. If the ice is warm and soft enough to permit
175 deformation such that the modelled surface ~~speedvelocity magnitude~~ is much faster
176 than the observed, then a friction inversion will be ineffective to correct this misfit,
177 producing a bias towards positive misfits (i.e., model velocities are too fast) in the
178 inversion results. Therefore, we use the positive difference between ~~the~~ simulated
179 ~~surface ice speed~~ and ~~the~~ observed ~~speedsurface velocity magnitude~~ to calculate the
180 inconsistency caused by the overheating effect:

$$AOH = \max(0, U_{sm} - U_{obs}), \quad (2)$$

181 where AOH refers to absolute overheating, U_{sm} represents the modelled surface ~~ice~~
182 ~~speedvelocity magnitude~~ and U_{obs} is the observed surface ~~ice speedvelocity magnitude~~.
183 We only calculated AOH for the thawed-bedded areas, i.e. $T_{bm} = T_{melt}$, because
184 observed surface ~~ice speedvelocity magnitude~~ errors are proportionally much less in
185 thawed-bedded areas (corresponding to fast flow regions) than in frozen-bedded area
186 (correspond to slow flow regions).

187 To mitigate the impact of substantial differences in observed surface ~~ice~~
188 ~~speedvelocity magnitude~~ across various areas, we also define "relative overheating"
189 (ROH) and "relative overcooling" (ROC), dividing AOH and AOC by the observed
190 surface ~~ice speedvelocity magnitude~~ respectively:

193
$$ROH = \frac{\max(0, U_{sm} - U_{obs})}{U_{obs}}, \quad (3)$$

194
$$ROC = (T_{melt} - T_{bm}) \times \frac{U_{bm}}{U_{obs}}. \quad (4)$$

195
196 **2.1.2 Normalization and ranking**

197 Overheating and overcooling inconsistencies are calculated on thawed bed and
198 frozen bed, respectively. To evaluate the inconsistencies for the whole domain, we
199 linearly normalized the overheating inconsistency and overcooling inconsistency to
200 range from 0 to 1 and then sum them as:

201
$$ACI = L_N(AOC) + L_N(AOH), \quad (5)$$

202
$$RCI = L_N(ROC) + L_N(ROH), \quad (6)$$

203 where ACI means absolute combined inconsistency, RCI represents relative combined
204 inconsistency, and L_N represents linear normalization. Taking AOC as an example, its
205 linear normalization is:

206
$$L_N(AOC) = \frac{AOC - AOC_{min}}{AOC_{max} - AOC_{min}}. \quad (7)$$

207 Therefore, we obtain ~~6 metrics consisting of~~ three absolute inconsistencies (AOH, AOC,
208 ACI) and three relative inconsistencies (ROH, ROC, RCI).

209 ~~These 6 indicators, with which we~~ can comprehensively analyze the temperature-
210 sliding inconsistency in the inversion results of ice sheet model. For each metric, we
211 rank the eight GHF datasets from 1 (least inconsistent) to 8 (most inconsistent). The
212 final score for each dataset is the average of its ranks across the six metrics to ensure a
213 comprehensive evaluation, as a reasonable simulation result should perform well across
214 thawed bed, frozen bed, and the whole region. We only consider grounded ice and
215 exclude points located at the domain boundary due to relatively poor model
216 performance there.

217 The specific metrics that we use to quantify this inconsistency could be adaptable,
218 for example by using a squared error term instead of the linear error terms that we used.
219 However, the general practice of emphasizing and quantifying the inconsistency
220 between a sliding inversion and the temperature/rheology field used as an input to that
221 inversion is novel.

222
223 **2.2 Methodology in Huang et al. (2024)**

224 ~~In this study, we validate our method by comparing our ranking of GHF datasets
225 to the observationally constrained ranking established by Huang et al. (2024). For
226 readers not familiar with this paper, we provide here a brief summary of their method
227 and, in the next section, clarify the distinction between their paper and the present study.~~

228 Huang et al. (2024) employed thermo-mechanical coupled simulations using eight
229 GHF datasets to investigate the steady-state thermal regime of Totten Glacier. The
230 methodology comprised two interconnected modeling components:

- 231 1. Forward Modeling: An enhanced shallow-ice approximation model integrated with
232 a subglacial hydrology module was utilized to simulate englacial temperature profiles.
- 233 2. Inverse Problem: A full-Stokes ice flow model was applied to resolve the basal
234 friction coefficients through inverse analysis, to minimize the misfit between simulated
235 and observed velocities while simultaneously generating velocity predictions.

236 A feedback loop was then established: the velocity outputs from the inverse model
237 were used to refine key parameters in the forward model - specifically constraining the
238 basal slip ratio, rheological properties, and shape functions. This bidirectional coupling
239 process underwent multiple iterations to achieve convergent steady-state solutions.

240 Huang et al. (2024) utilized radar specularity content data to differentiate localized
241 wet (thawed) versus dry (frozen) basal conditions and used this data as a two-sided
242 constraint on the basal thermal state. They compared modeled basal thermal states
243 derived from different GHFs to evaluate the reliability of the GHF datasets.

244 2.3 Distinction from Huang et al. (2024)

245 In Huang et al. (2024), modelled surface velocity velocities are compared with
246 observations over the whole domain during the inversion for basal parameters for each
247 GHF dataset. Here, surface velocities act as the observational constraints for the
248 mechanical inversion.

249 Although the overheating metrics here use the surface velocities and can thus be
250 considered a subset of the inversion residual, our overcooling metrics are based on the
251 basal sliding velocity derived from the inversion, which is not part of the mechanical
252 inversion's residual. A mechanical inversion does not take into account the physical
253 plausibility of the sliding result it produces. Therefore, it is not circular reasoning to
254 compare two different parts of a model to each other; rather, it is a cheekan assessment
255 of internal consistency, or lack thereof. A mechanical inversion may fit the surface
256 velocity observations equally well when forced with many different models of the ice
257 sheet thermal structure and rheology; however, if some models require high sliding
258 velocities in frozen-based regions, then they should be downweighted in comparison to
259 models that show a good agreement between basal temperature and velocity.

260 The method here does not require any additional observations beyond the surface
261 velocities used in the mechanical inversion. However, there are “independent
262 constraints” in the method here, which are not observations, but rather the a priori
263 physical understandings that: 1) rapid sliding requires warm basal temperatures and
264 subglacial water; 2) reducing the basal slip coefficient cannot prevent the ice from
265 flowing by internal shear deformation. The inconsistency metrics developed in this

267 paper are an attempt to quantify and rank the extent to which these basic (and
268 uncontroversial) physical understandings are violated.

269

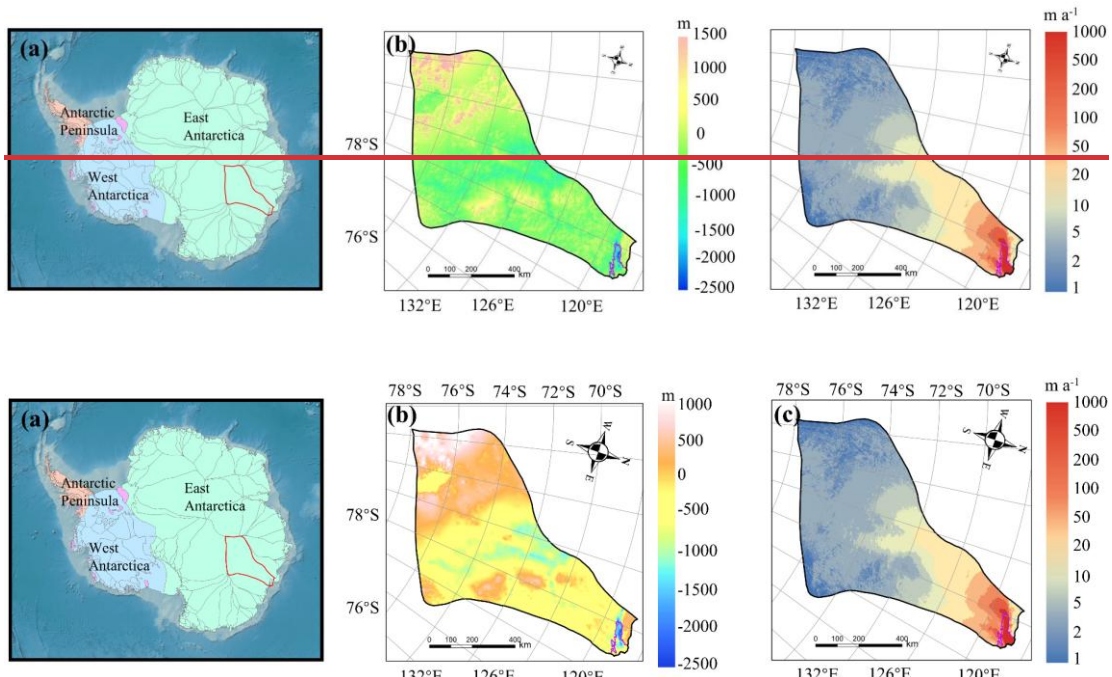
270 3. Application to Totten Glacier with Different GHFs

271 3.1 Study domain and Data

272 We apply our method to evaluate simulated ice temperature and ice velocity in
273 Totten Glacier with eight GHF datasets by Huang et al. (2024).¹ Huang et al. (2024)
274 used the present-day surface ice temperature (Le Brocq et al., 2010), observed surface
275 velocity from MEASUREs InSAR-Based Antarctic Ice Velocity Map, version 2 (Rignot
276 et al., 2017) and ice sheet topography data from BedMachine Antarctica, version 2
277 (Morlighem et al., 2020). The eight GHF datasets were derived by various
278 methodologies, resulting in significant differences in both spatial distribution and
279 magnitude (Fig. 2). GHF fields from Stål et al. (2021), Haeger et al. (2022), Lösing and
280 Ebbing (2021) and Martos et al. (2017) generally exhibit higher magnitudes than the
281 other GHFs. [Table S1 summarizes the input datasets, which follows the configuration](#)
282 [described in Huang et al. \(2024\).](#)

283

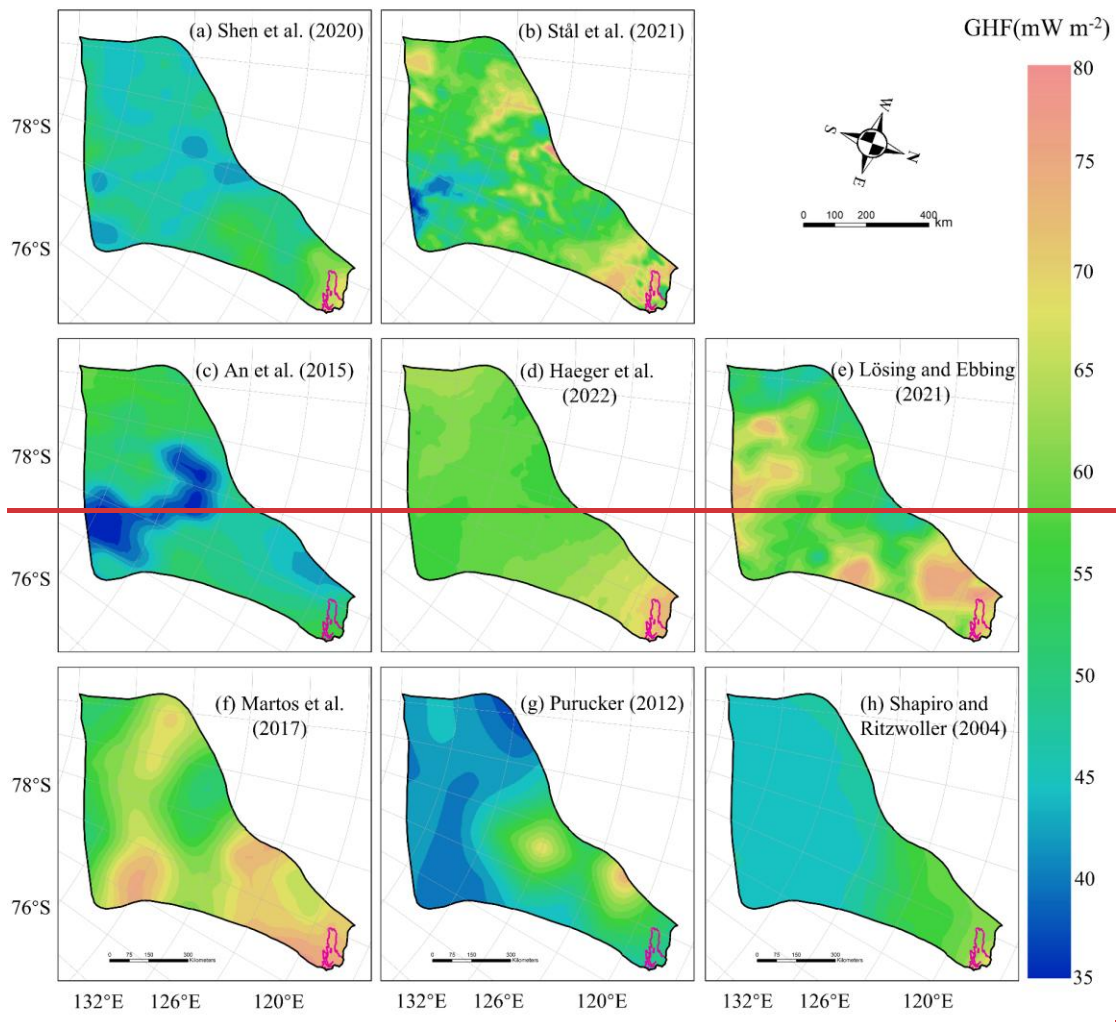
284

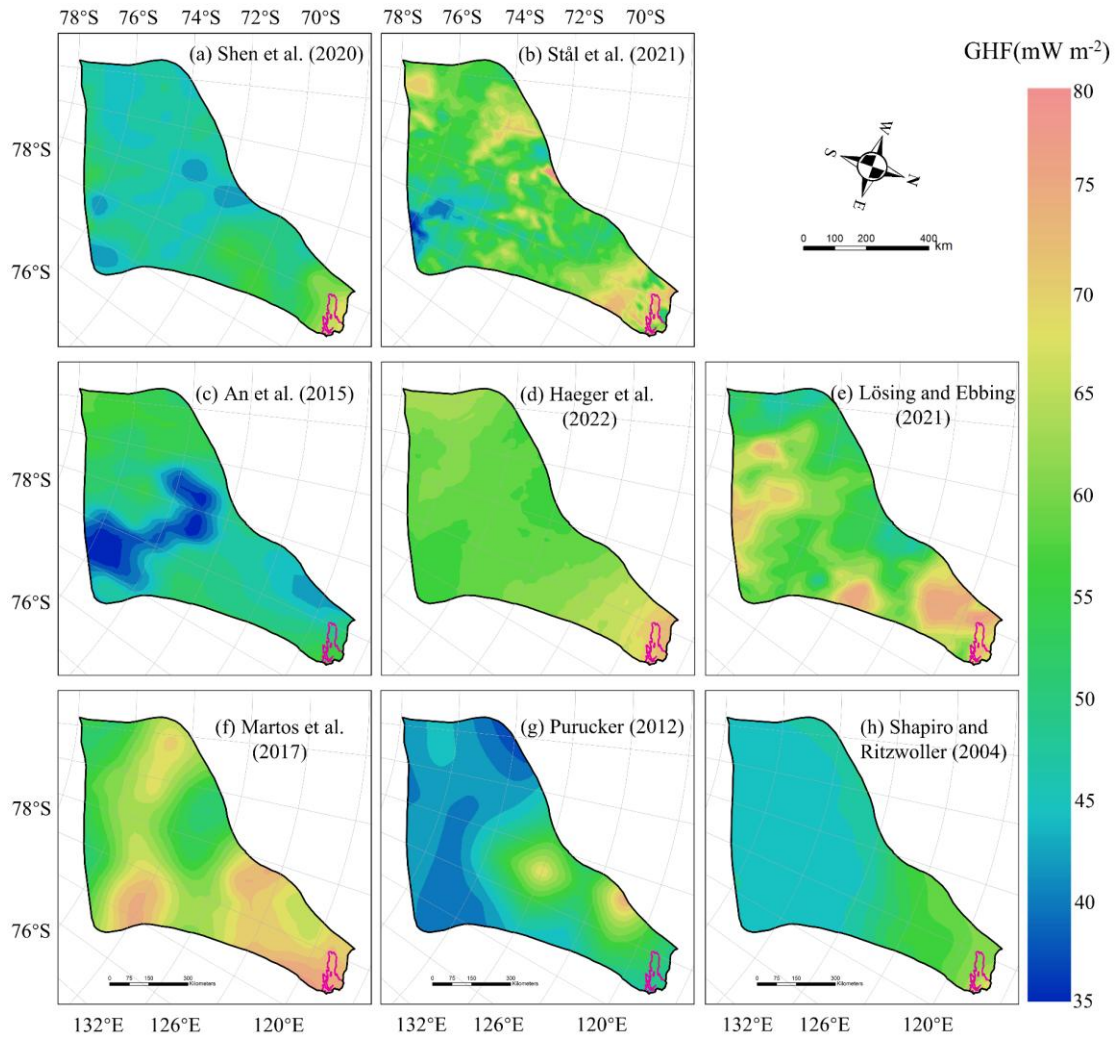


285

286 **Figure 1.** (a) Geographic location of Totten Glacier (red outline) in Antarctica; (b) bed
287 elevation of Totten Glacier, the purple curve represents the grounding line; (c) observed
288 surface velocity.

289





291

292 **Figure 2.** The spatial distribution of the 8 GHF datasets for Totten Glacier (a–h) used
 293 as input data in Huang et al. (2024). The purple line depicts the grounding line.

294

295 The spatial distribution of modelled basal temperature using the 8 GHFs displays
 296 both similarities and heterogeneity. In the northern part of Totten Glacier, there is a
 297 consistent thawed-bedded pattern across all eight simulation results (Fig. S1), which
 298 originates from the grounding line and extends upstream to approximately 71°S. This
 299 thawed-bedded area is not contiguous with the lateral boundaries of Totten Glacier but
 300 is instead bordered by frozen bed. All 8 GHF datasets produce low basal ice
 301 temperatures in the inland southwest, with Purucker et al. (2012), Shapiro and
 302 Ritzwoller (2004), Shen et al. (2020) and Lösing and Ebbing (2021) being colder. than
 303 the other four GHF products. The basal ice velocities modelled from the 8 different
 304 GHF datasets produce similar spatial distributions (Fig. S2), which can be expected as

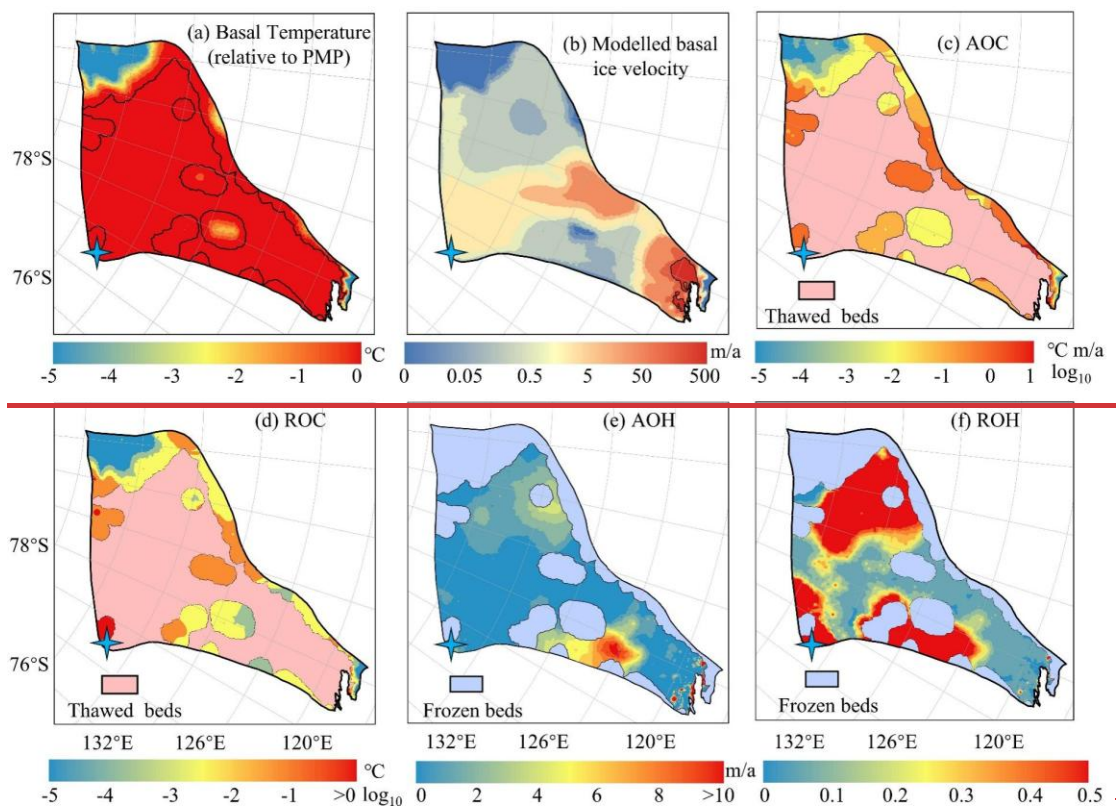
305 they were derived using the same inverse method and constrained by the identical
 306 observed surface ice velocity. The modelled basal ice velocity is fast near the grounding
 307 line and its upstream area. There are also high velocities between 70°S and 72°S close
 308 to the western boundary of Totten Glacier (Fig. 1c), which are associated with
 309 subglacial canyon features in the basal topography (Fig. 1b) and observed fast surface
 310 ice velocity there.

311

312 3.2 Spatial Distribution of Inconsistencies with one GHF dataset

313 In this section, we show the spatial fields of the inconsistency metrics (Section 2.1)
 314 for the modelled result in Huang et al. (2024), using Martos et al. (2017) GHF as an
 315 example. This example illustrates the interpretation process before conducting a
 316 comprehensive comparative analysis for the result with 8 GHF datasets.

317



318

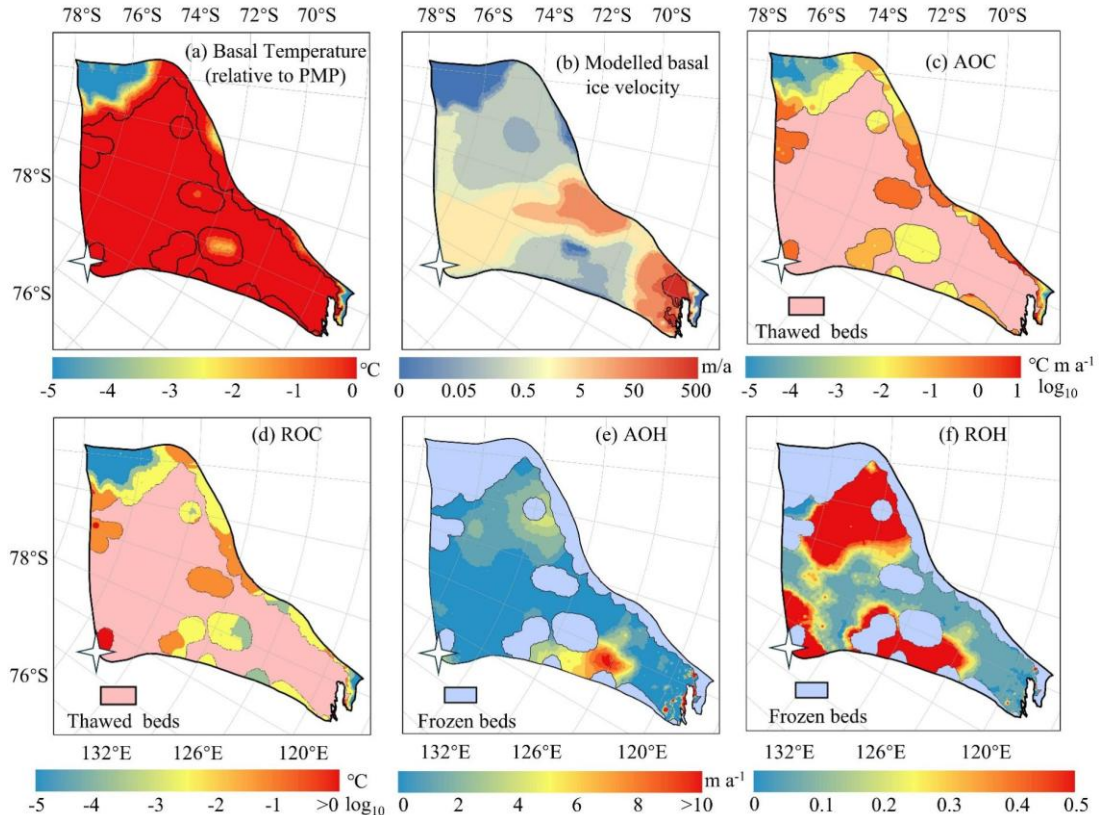


Figure 3. Spatial distribution of modelled basal ice temperature (a), modelled basal ice speedvelocity magnitude (b), AOC (c), ROC (d) inconsistencies in modelled frozen-bedded regions, and AOH (e) and ROH (f) inconsistencies in modelled thawed-bedded regions associated with Martos et al. (2017) GHF. The colormap in (c) and (d) is on logarithmic scale. The pink region in (c) and (d) represents modelled thawed bed, while the blue region in (e) and (f) indicates frozen-bedded areas. The white star represents Dome C.

The modelled result based on the Martos et al. (2017) GHF reveals extensive regions of thawed bed with limited areas of frozen bed. The frozen bed is predominantly located in the southern corner of the study domain, where the modelled basal ice speedvelocity magnitude approaches zero, consistent with cold basal ice temperature. Consequently, the AOC inconsistency at this marginal zone is negligible (Fig. 3). Along the western margin of Totten Glacier, basal ice temperature remains below the pressure melting point, albeit approaching it. However, localized regions exhibit high basal velocities of several tens of meters per year, contradicting the presence of a frozen bed and resulting in large AOC inconsistencies.

Conversely, large AOH values are observed between 69°S and 71°S in the eastern Totten Glacier region, where the simulated surface ice speedvelocity magnitude

339 exceeds observational data by >5 m a $^{-1}$ (Fig. 3e). In this area, the modelled basal ice
340 temperature reaches the pressure melting point, with the modelled basal ~~ice~~
341 ~~speed~~~~velocity~~ ~~magnitude~~ at approximately 0.05 m a $^{-1}$. Basal friction inversion failed to
342 reproduce observed surface ~~ice~~~~speed~~~~velocity~~ ~~magnitude~~ due to the model's
343 overestimation of ice temperature and softness. This pronounced velocity mismatch
344 highlights a fundamental inconsistency in the eastern glacier region, likely originating
345 from discrepancies in the input datasets. Regions of high ROH and ROC values
346 coincide with areas of relatively high AOH and AOC, particularly where the observed
347 surface velocities are slow, as per their formulations.

348

349 **3.3 Spatial Distribution of Inconsistencies with eight GHF datasets**

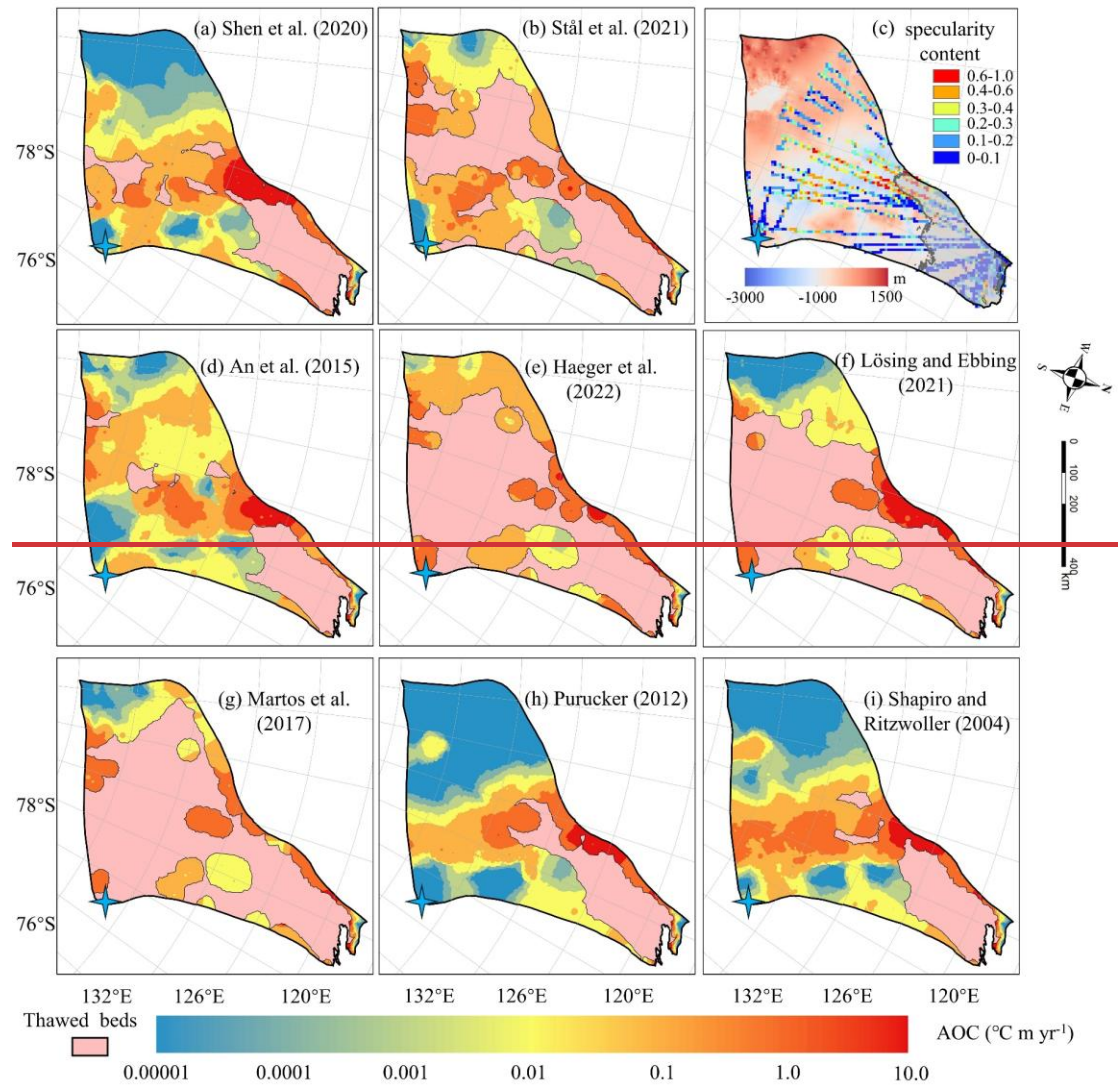
350 ~~We calculate the absolute inconsistencies, AOH, in the thawed bed, and AOC in the~~
351 ~~frozen bed.~~

352 **3.3.1 Overcooling Inconsistency on Frozen Beds**

353 ~~We calculated the inconsistency metrics for the thawed and frozen beds~~
354 ~~respectively, and summed the values over the corresponding regions. The results are~~
355 ~~shown in Table 1. To visualize the spatial heterogeneity of these inconsistencies, we~~
356 ~~mapped the distribution of the metrics.~~ The spatial distribution of AOC reveals that
357 most GHF datasets exhibit significant local overcooling inconsistencies at the
358 subglacial canyon between 70°S and 72°S (Fig. 4). There is fast basal sliding in the
359 inverse model results (Fig. S2), however, the modelled basal ice temperatures inferred
360 from most of the GHF datasets are below the pressure melting point (Fig. S1). High
361 specularity content in radar data (Fig. 4c) suggests the presence of basal water in the
362 subglacial canyons here (Dow et al., 2020; Huang et al., 2024), which also suggests that
363 the basal ice temperature should be at the pressure melting point and confirms the
364 inconsistency between the modelled temperature and velocity fields.

365 The area near the grounding line is characterized by fast ice flow (Fig. S2) and
366 thawed bed (Fig. 4), yet some of the margin is frozen-bedded with modelled basal
367 temperature below the pressure melting point, resulting in high AOC. Overall, modelled
368 results with most GHF datasets show small overcooling inconsistencies. The modelled
369 results using GHF from Purucker et al. (2012), Shapiro and Ritzwoller (2004), Shen et
370 al. (2020), Lösing and Ebbing (2021) exhibit no overcooling inconsistency in
371 southwestern Totten Glacier (Fig. 4). ~~The largest value of ROC across most GHF occurs~~
372 ~~at Dome C (white star in Figure 5), where the observed surface ice velocity magnitude~~
373 ~~is close to zero (Fig. 1c).~~

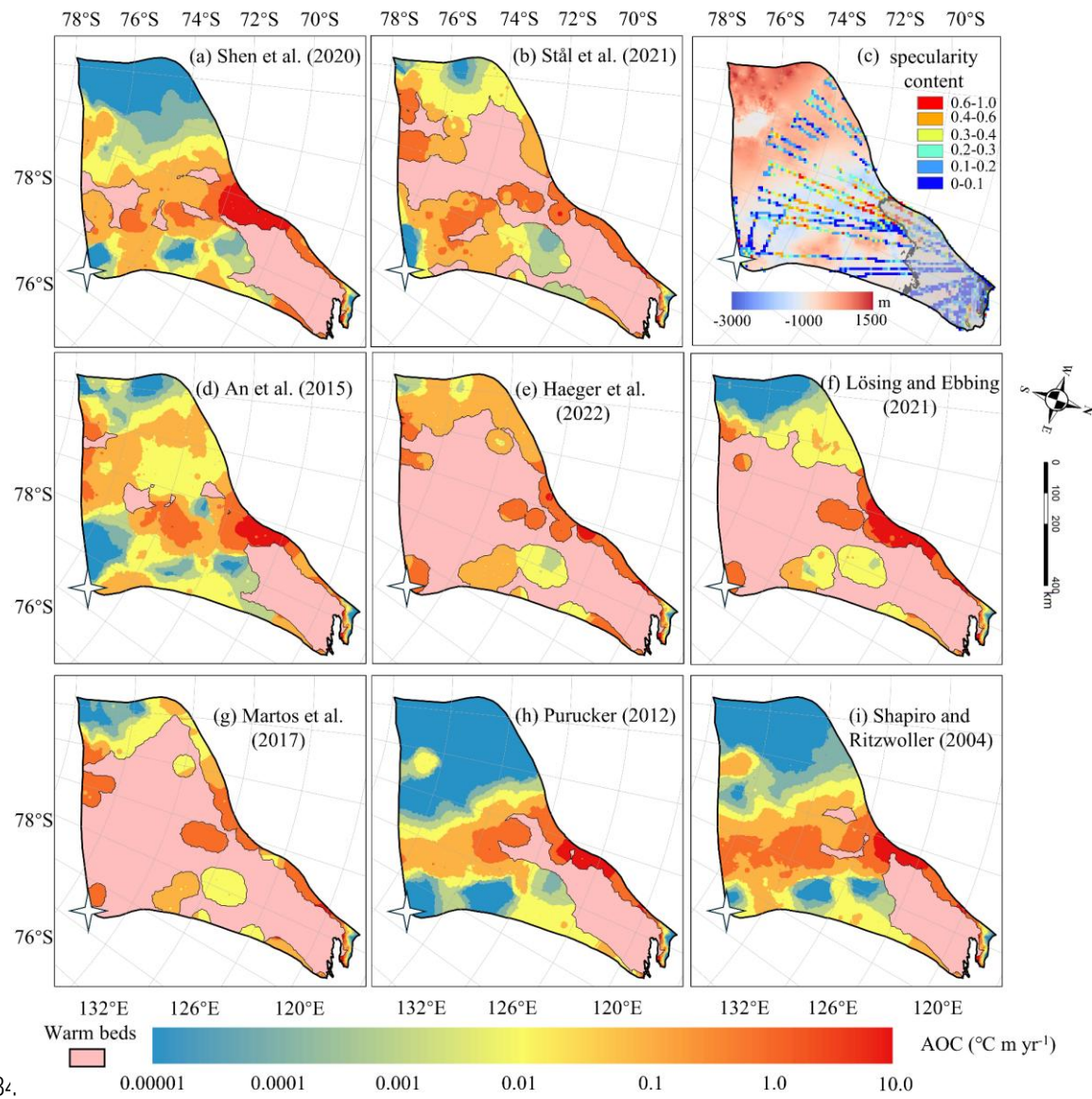
374 ~~The spatial distribution of relative overcooling inconsistencies, ROC (Fig. 5),~~
375 ~~differs from that of absolute inconsistencies, AOC, and is due to the spatial variability~~
376 ~~in surface ice speed. The largest value of ROC across most GHF occurs at Dome C,~~
377 ~~where the observed surface ice speed is close to zero.~~

381 **Table 1. Summary of inconsistency metrics for different GHF maps.**

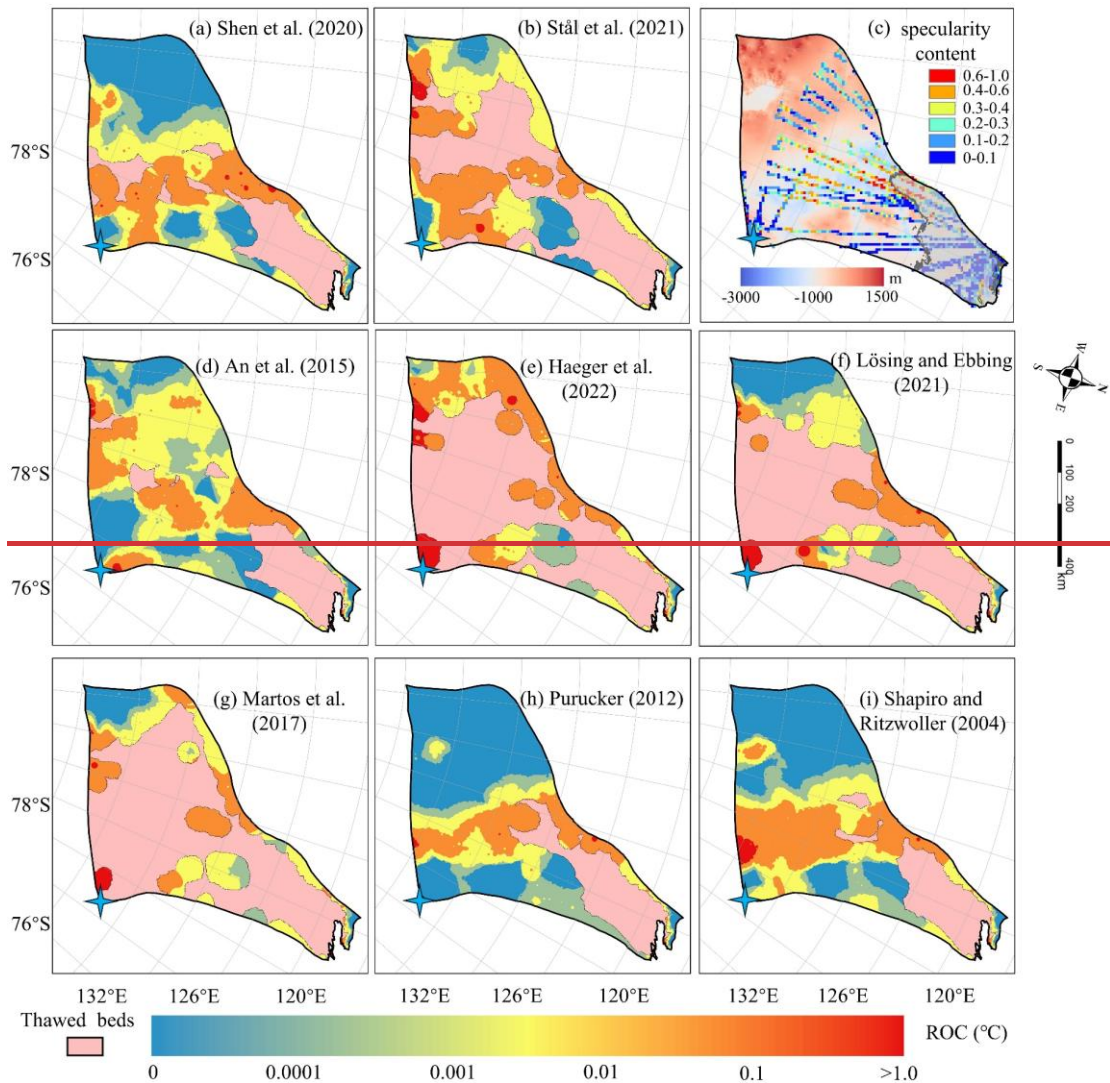
<u>GHF maps</u>	<u>AOC</u> (°C km yr ⁻¹)	<u>AOH</u> (km yr ⁻¹)	<u>ROC</u> (°C)	<u>ROH</u>	<u>ACI</u>	<u>RCI</u>
<u>Shen et al. (2020)</u>	<u>6.39</u>	<u>29</u>	<u>159</u>	<u>470</u>	<u>0.59</u>	<u>0.39</u>
<u>Stål et al. (2021)</u>	<u>6</u>	<u>31.9</u>	<u>144</u>	<u>814</u>	<u>0.84</u>	<u>0.8</u>
<u>An et al. (2015)</u>	<u>5.97</u>	<u>30.5</u>	<u>130</u>	<u>397</u>	<u>0.53</u>	<u>0.11</u>
<u>Haeger et al. (2022)</u>	<u>6.32</u>	<u>34.1</u>	<u>126</u>	<u>889</u>	<u>1.51</u>	<u>1.57</u>
<u>Lösing and Ebbing (2021)</u>	<u>6.91</u>	<u>34.1</u>	<u>290</u>	<u>780</u>	<u>1.97</u>	<u>1.58</u>
<u>Martos et al. (2017)</u>	<u>5.82</u>	<u>34.2</u>	<u>146</u>	<u>1072</u>	<u>1.14</u>	<u>1.18</u>
<u>Purucker (2012)</u>	<u>5.89</u>	<u>30.6</u>	<u>115</u>	<u>375</u>	<u>0.5</u>	<u>0</u>

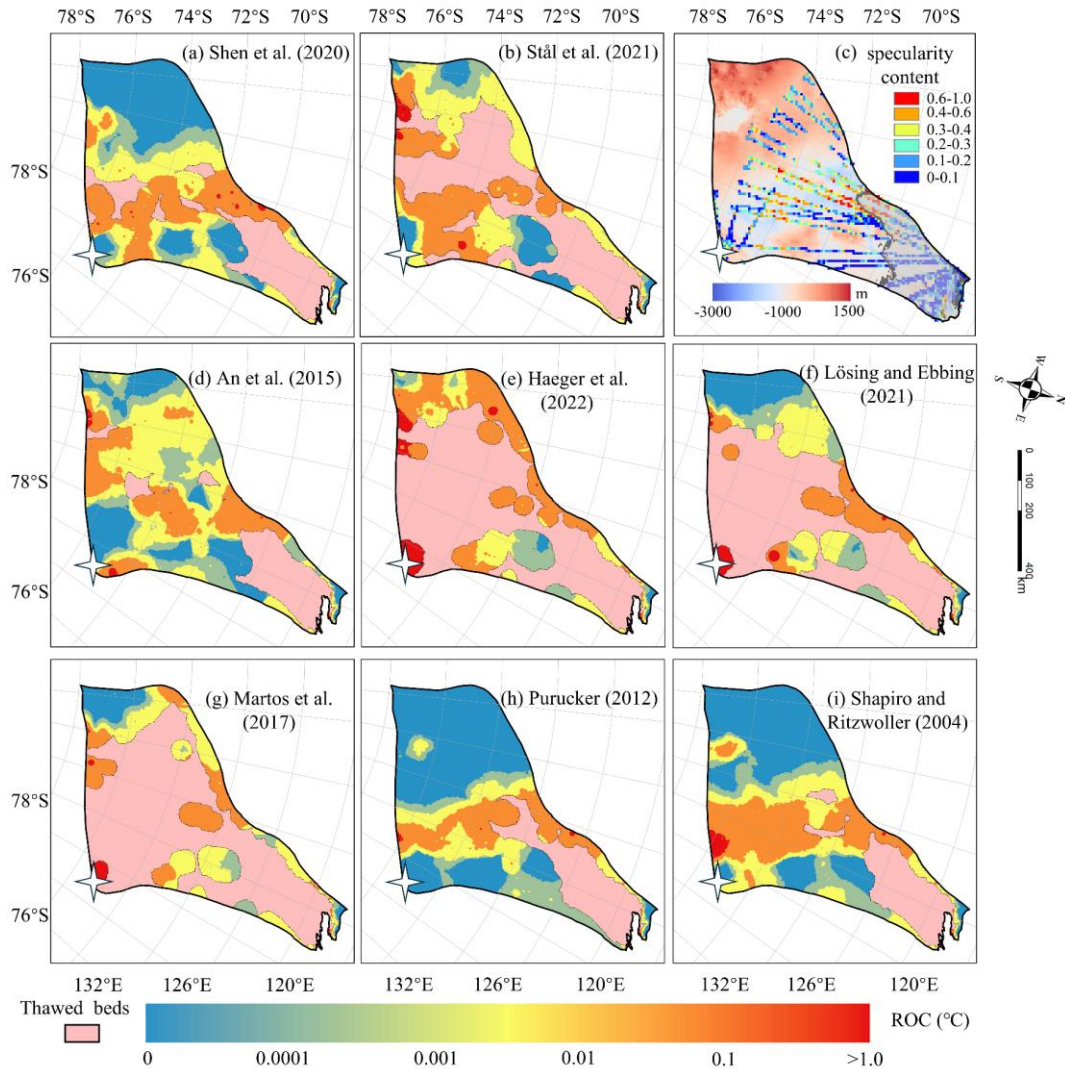
Shapiro and Ritzwoller (2004) 5.65 31.8 138 417 0.54 0.19

382
383



385 **Figure 4.** Spatial distribution of AOC inconsistency in modelled frozen-bedded regions
386 (a-b, d-i) associated with the GHFs (a-h) in Fig. 2. The colormap is on logarithmic
387 scale. The pink region represents modelled thawed bed. (c) Specularity content sourced
388 from radar data collected by ICECAP (Dow et al., 2020) with the bed elevation in the
389 background. Gray area in (c) corresponds to surface speedvelocity magnitude exceeding
390 30 m yr^{-1} . The bluewhite star represents Dome C. Note the colormap is logarithmic.
391

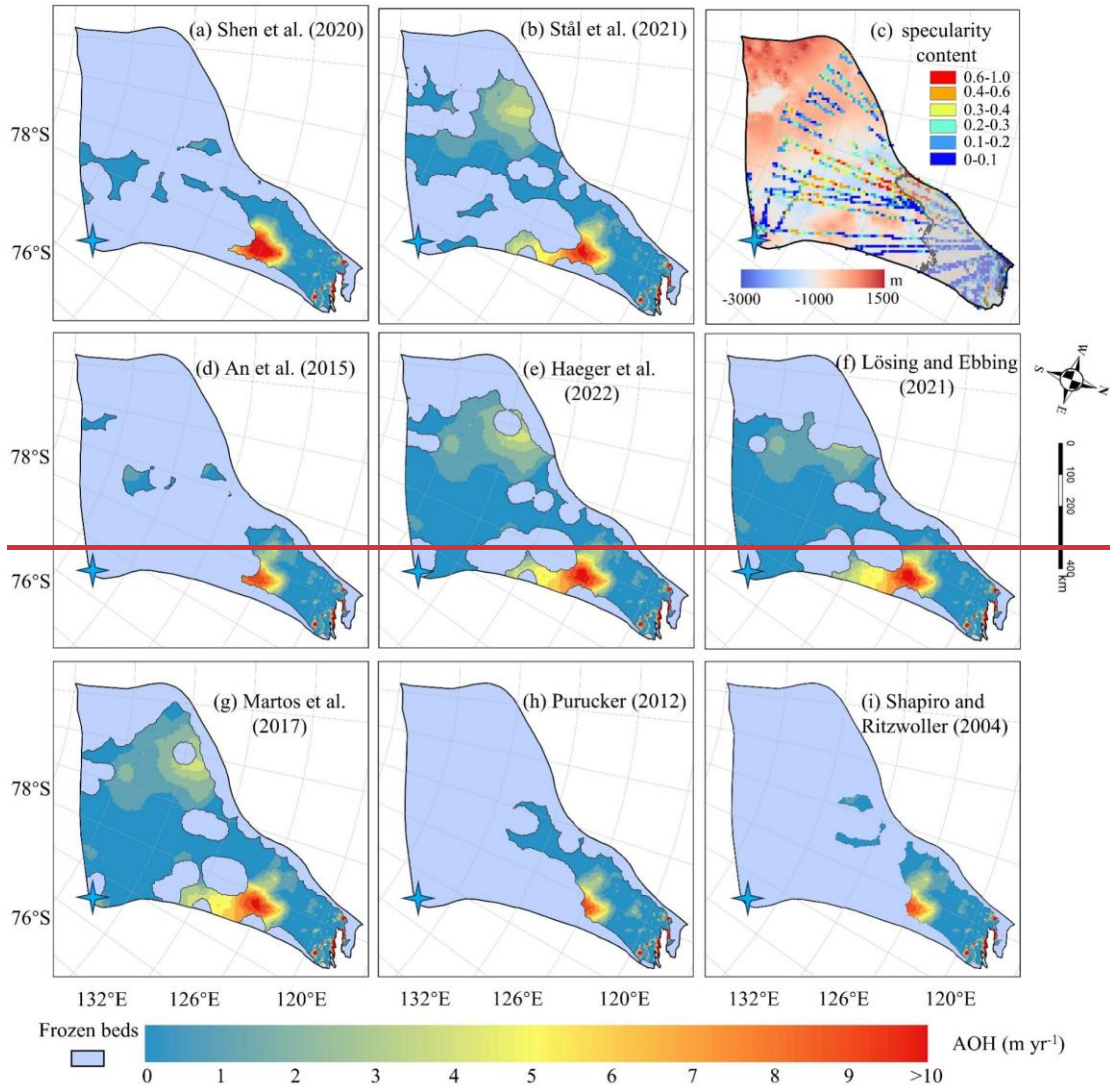




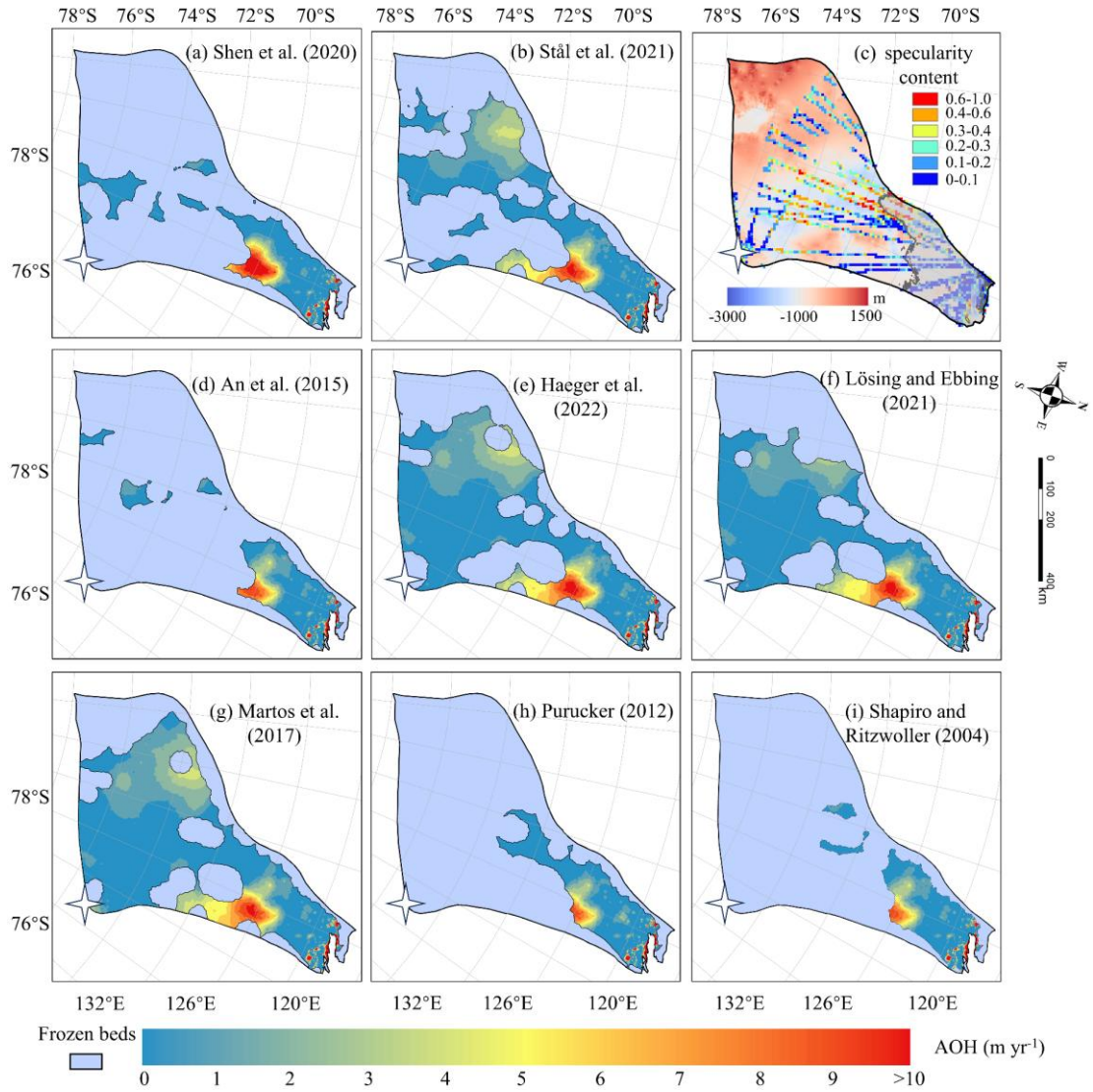
393 Figure 5. The spatial distribution of relative overcooling (ROC) inconsistency in cool
 394 beds with (a), (b) and (d) to (i) corresponding to the GHFs (a – h) in Figure 2. The pink
 395 area represents the thawed beds. Dome C is marked by a bluewhite star. (c) Locations
 396 of specularity content derived from radar data collected by ICECAP (Dow et al., 2020)
 397 and with the bed elevation in the background. The gray curve is the contour of the
 398 surface speedvelocity magnitude of 30 m yr^{-1} . Note the colormap is non
 399 linearlogarithmic.
 400

401
 402 The GHF datasets of Stål et al. (2021), Haeger et al. (2022), Lösing and Ebbing (2021)
 403 and Martos et al. (2017) which have higher than average GHF values provide larger
 404 areas of thawed bed than the other 4 GHFs. **3.3.2 Overheating Inconsistency on**
 405 **Thawed Beds**

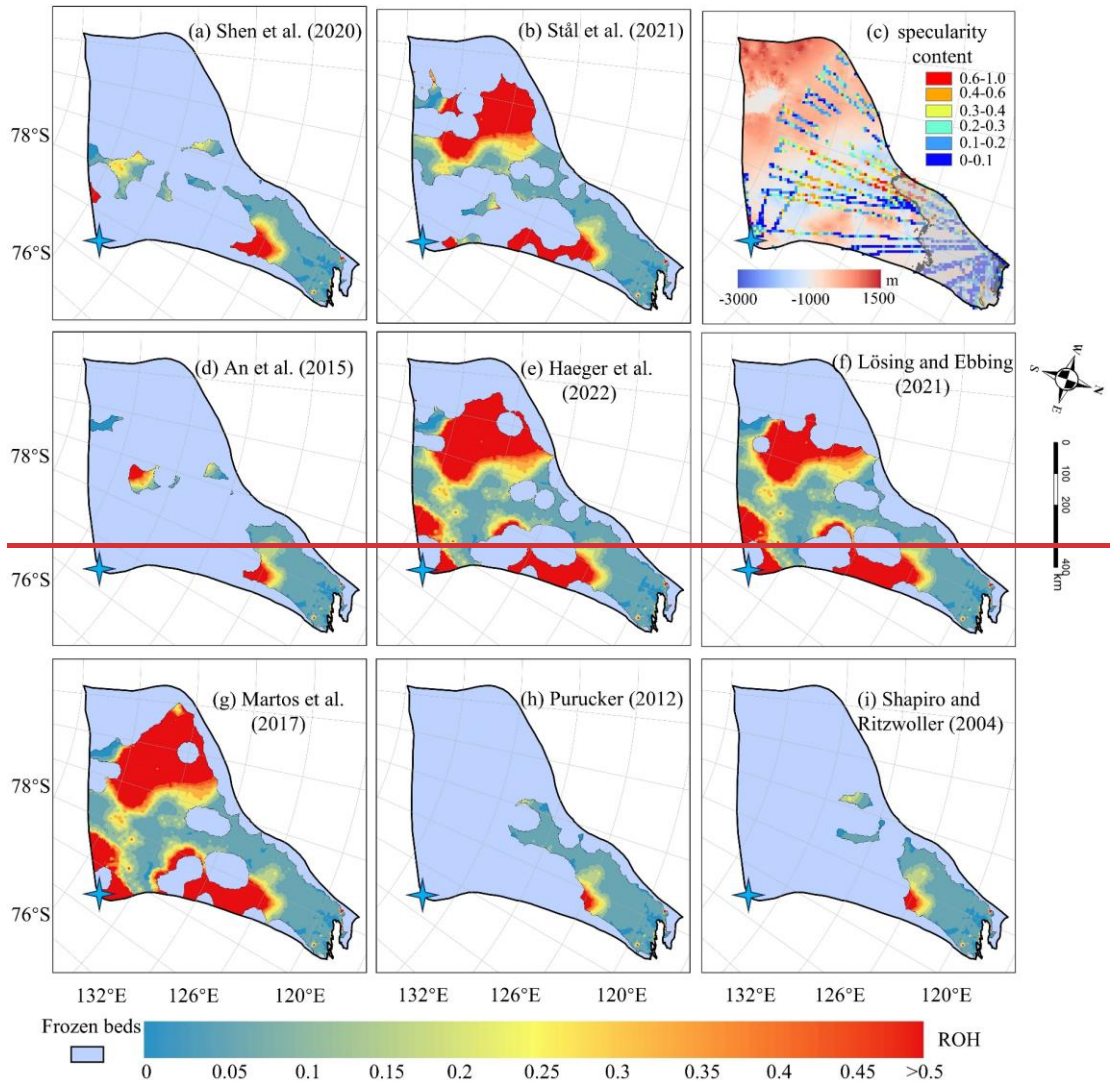
406 The simulations with all 8 GHFs yield similar spatial distributions of AOH (Fig. 407 6) on the common area of thawed bed, and similar locations of high AOH values. A 408 common high AOH area is located between 69°S and 72°S in the eastern part of Totten 409 Glacier, due to simulated surface ice velocities greatly exceeding the observed surface 410 ice velocities. Low specularity content from radar data (Fig. 6c) suggests there is no 411 basal water in the area (Dow et al., 2020; Huang et al., 2024). Therefore, it is likely that 412 the basal ice temperature is overestimated there. The simulations with all the 8 GHFs 413 also yield similar spatial distribution of ROH (Fig. 7), but its largest values are mostly 414 in the slow flowing region as one may expect from its formulation (Eq. (3)).

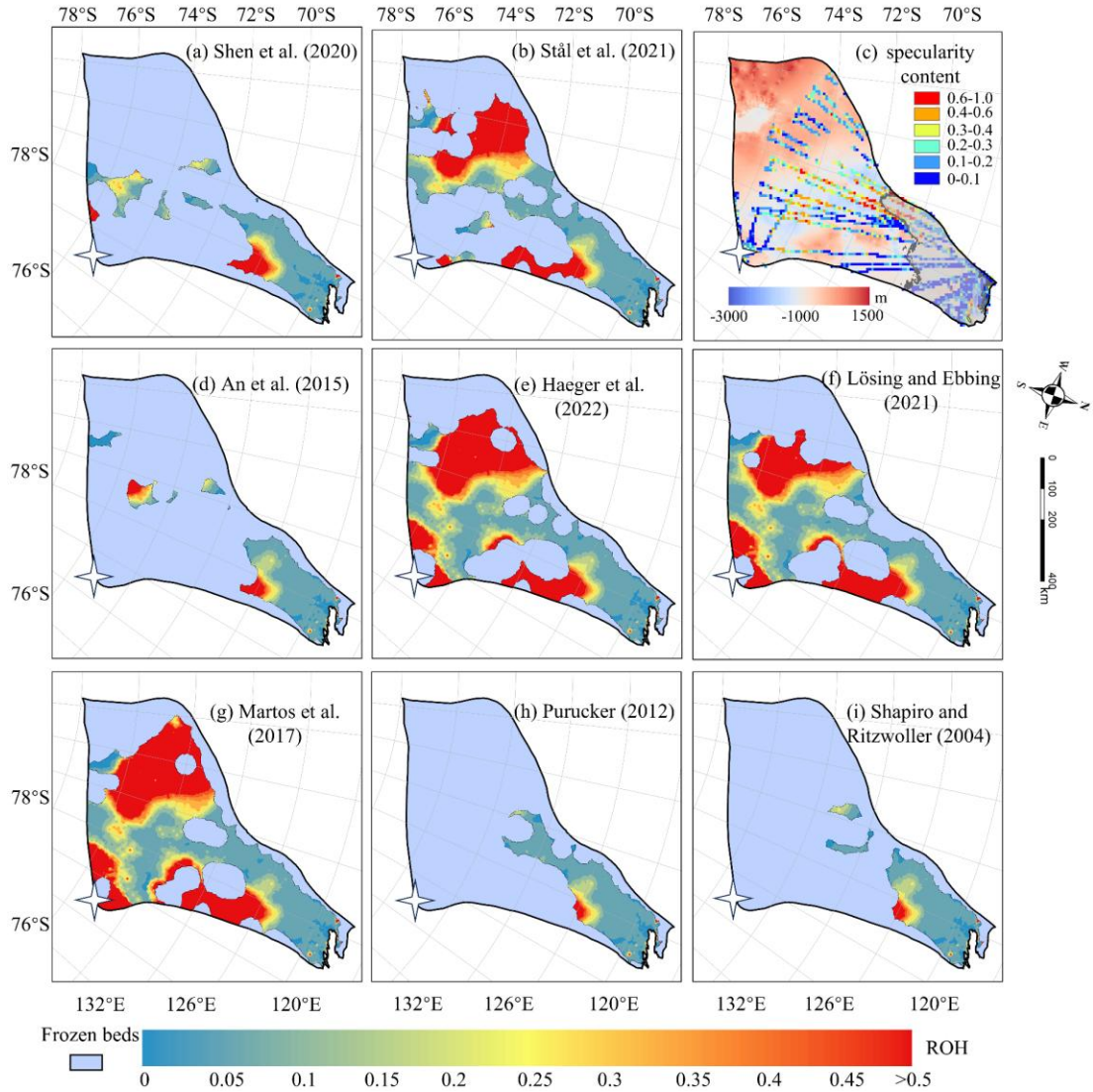


415



416 **Figure 6.** Spatial distribution of AOH in thawed-bedded regions with **(a-b, d-i)**
 417 corresponding to the GHFs **(a-h)** in Fig. 2. The blue region indicates frozen-bedded
 418 areas. **(c)** Locations of specularity content, same as Fig. 4c. The **bluewhite** star
 419 represents Dome C.
 420





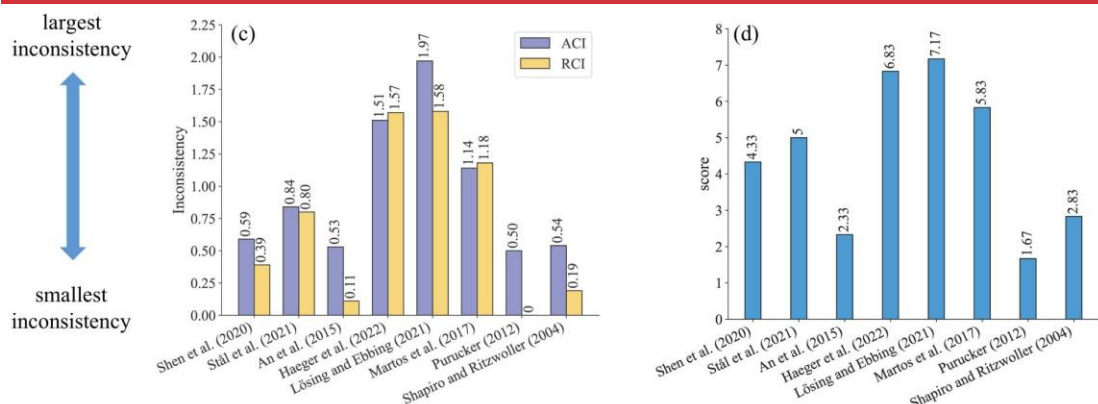
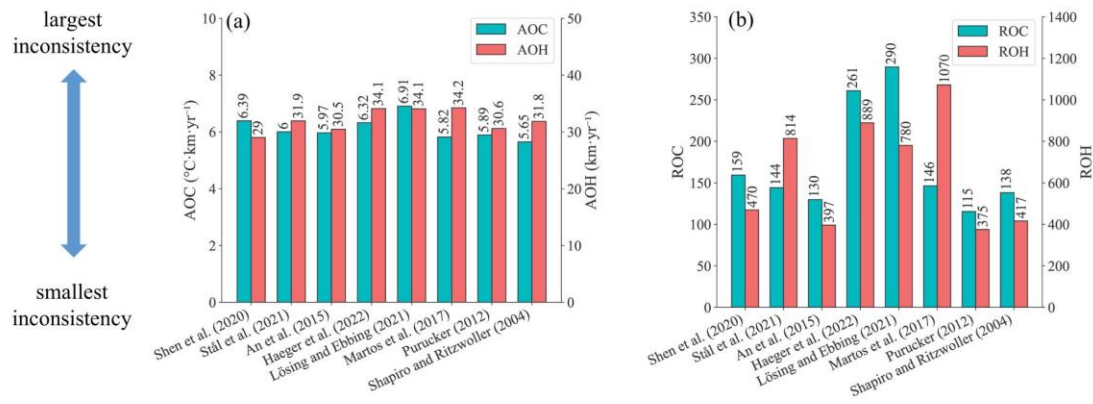
423
424 Figure 7. The spatial distribution of relative overheating (ROH) inconsistency in
425 thawed beds with (a), (b) and (d) to (i) corresponding to the GHFs (a - h) in Figure 2.
426 The light purple mask represents the frozen beds. (c) Locations of specularity content
427 (coloured points), same as Fig. 6. The white star represents Dome C.

428 429 3.4 Evaluation of Model Inconsistency with Eight GHFs

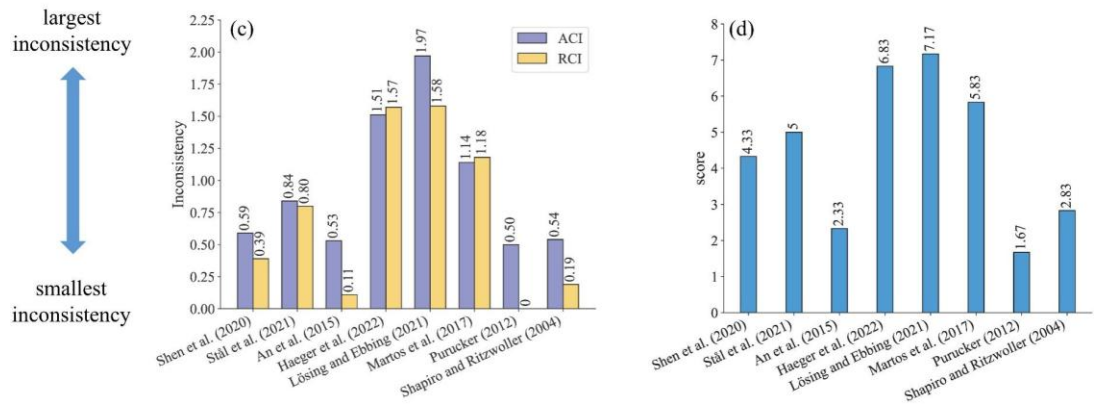
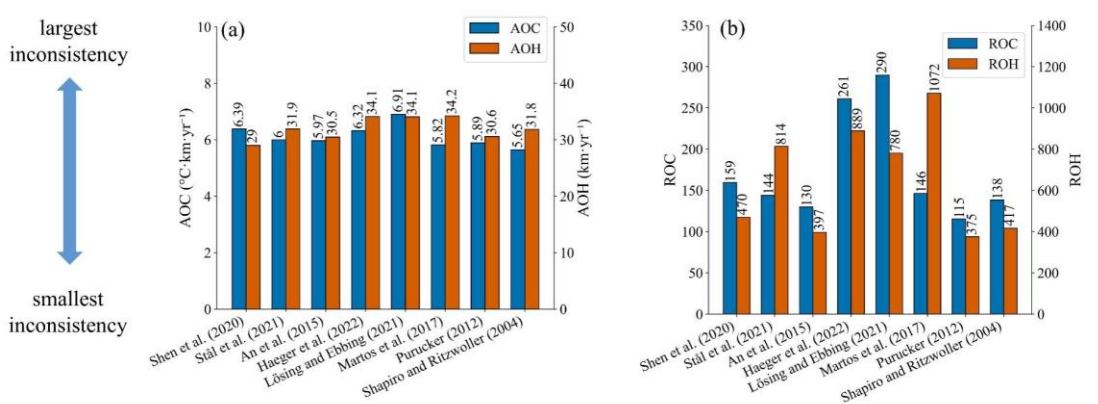
430 To assess the overall inconsistency of each geothermal heat flux dataset, we
431 calculate the sum of each metric over all points. All inconsistency indices for the
432 simulation results using the eight GHF datasets are illustrated in Fig. 8. The overheating
433 inconsistency associated with Purucker et al. (2012) and Shapiro and Ritzwoller (2004)
434 GHFs is predominantly localized in fast-flowing regions. Consequently, after
435 normalization by the ~~surface~~ observed ~~ice speed~~ ~~surface velocity magnitude~~, their

436 relative rankings improve (Fig. 8). The GHFs from Purucker et al. (2012), An et al.
437 (2015), Shapiro and Ritzwoller (2004), and Shen et al. (2020) demonstrate balanced
438 performance with respect to both overheating and overcooling inconsistency metrics,
439 thereby securing the top four positions in both ACI and RCI. Their ACI values exhibit
440 similarity, ranging from 0.50 to 0.59 (Fig. 8c). In contrast, simulation result utilizing
441 Martos et al. (2017) GHF exhibits low AOC but high AOH. Simulation results utilizing
442 Stål et al. (2021) GHF show low ROC but relatively high ROH. Notably, simulation
443 results employing GHFs from Martos et al. (2017), Haeger et al. (2022), and Lösing
444 and Ebbing (2021) demonstrate comparably high AOH values. These four GHF
445 datasets—Martos et al. (2017), Stål et al. (2021), Haeger et al. (2022), and Lösing and
446 Ebbing (2021)—are ranked in the bottom four positions for both ACI and RCI metrics.
447 Furthermore, the ranking order of the eight GHFs remains consistent between ACI and
448 RCI.

449 The final averaged ranking (Fig. 8d) across the indices is also the same as that of
450 ACI and RCI. Purucker et al. (2012), An et al. (2015) and Shapiro and Ritzwoller (2004)
451 GHFs occupy the top three positions. Following closely, Shen et al. (2020) and Stål et
452 al. (2021) GHFs secure the 4th and 5th positions, respectively. Martos et al. (2017),
453 Haeger et al. (2022) and Lösing and Ebbing (2021) GHFs are ranked as the bottom
454 three among the eight GHFs in Totten Glacier. The thermal state produced by the
455 optimal GHF result shows that thawed beds predominantly cluster around the
456 grounding line and its upstream regions. Conversely, the inland areas of Totten largely
457 exhibit cold temperatures, with relatively sparse thawed-bedded areas.



458



459

460 **Figure 8.** Six inconsistency indicators and the final ranking of 8 GHF datasets. **(a)** the
461 absolute overcooling and overheating inconsistencies, AOC and AOH; **(b)** the relative
462 overcooling and overheating inconsistencies, ROC and ROH; **(c)** the absolute and
463 relative combined inconsistencies, ACI and RCI; **(d)** the average of ranking scores from
464 1 to 8 using the six inconsistency indicators. The value of inconsistencies and scores
465 are labeled at the top of the bars.

466

467 **4. Discussion**

468 **4.1 Sensitivity of Inconsistencies to GHF Datasets**

469 Comparing the GHF dataset rankings between this study and Huang et al. (2024),
470 we find that the top 4 and the bottom 4 are the same in the two studies, albeit with slight
471 variations in ranking. The lower ranking of Shen et al. (2020) in this study may be
472 attributed to several factors. Firstly, Huang et al. (2024) excludes areas with ice velocity
473 magnitude exceeding 30 m a^{-1} (Fig. 4c) because specularity content is an ambiguous
474 indicator of wet beds there. Secondly, the GHF from Shen et al. (2020) yields higher
475 basal temperature and also faster basal ice velocities in most of the frozen bed of Totten
476 Glacier, hence exhibits greater overcooling inconsistency, compared with Purucker et
477 al. (2012), leading to a decrease in its rankings (Fig. S3). Lastly, Huang et al. (2024)
478 primarily relied on specularity content, while our study evaluated datasets based on
479 inconsistencies in the simulation results. Despite these methodological differences, both
480 studies identified four relatively well-performing GHF datasets for Totten Glacier,
481 which exhibit similar distributions of thawed and frozen beds when compared to the
482 other four datasets (Fig. 4 and Fig. 6). This similarity underscores that the thawed bed
483 is concentrated near and upstream of the grounding line. Datasets from Stål et al. (2021),
484 Martos et al. (2017), Haeger et al. (2022), and Lösing and Ebbing (2021) exhibit a
485 tendency to overestimate GHF in central Totten Glacier.

486 Simulations employing GHF datasets from Stål et al. (2021), Martos et al. (2017),
487 Haeger et al. (2022), and Lösing and Ebbing (2021) yield more extensive thawed-
488 bedded regions and are expected to exhibit greater overheating inconsistency.
489 Nevertheless, these models also exhibit relatively high overcooling inconsistency
490 despite the limited extent of frozen-bedded regions. We quantified the discrepancies
491 between these four GHF datasets and the Purucker et al. (2012) GHF in terms of
492 modelled basal velocity, basal temperature relative to the pressure melting point, and
493 AOC (Fig. S4). The Purucker et al. (2012) GHF yields lower basal ice temperatures and
494 slower basal velocities across most frozen-bedded regions, consequently resulting in
495 lower AOC values compared to the other four GHF datasets.

496

497 **4.14.2 Causes of Inconsistencies and Sources of Uncertainty**

498 Our method evaluates the quality of an ice sheet temperature field by quantifying
499 the inconsistency between that temperature field and the velocity field that is obtained
500 if that temperature field is used to compute the rheology in a mechanical inversion.
501 Because mechanical inversions use surface velocity observations as a constraint, we
502 have developed an indirect method for using surface velocity observations to check the
503 quality of an englacial temperature simulation. We have developed an indirect method
504 that utilizes surface velocity observations to assess the quality of simulated basal
505 temperature. However, the mere fact that inconsistencies exist does not by itself tell us
506 what caused those inconsistencies.

507 Broadly speaking, the measured inconsistencies can come from two sources:
508 temperature or velocity. Uncertainties in any of the input datasets used to compute those
509 two fields can produce inconsistencies, as can simplifications in the model physics.
510 Here, we have tested the influence of one particular boundary condition, GHF, since
511 that field is particularly hard to constrain. Because all other inputs are kept constant,
512 the differences in the inconsistencies that we calculated between different simulations
513 can be attributed to the GHF fields. However, we also found that all of the models we
514 tested had non-zero inconsistency (Fig. 4; Fig. 6). The absolute inconsistencies, AOH
515 and AOC, had particularly small between-model variability in comparison to their mean
516 value. This could be because none of related to uncertainties or limitations in the input
517 GHF fields correctly captured the true GHF, but it could also indicate problems
518 with sensitivities to other model inputs. For instance, the surface temperature used in
519 Huang et al. (2024) represents the present-day climate, but the thermal structure of the
520 ice sheet may reflect colder temperatures during the last glacial cycle. We discuss an
521 additional experiment we performed to test the influence of uncertainty in surface
522 temperature on our inconsistency metrics in Section 4.3 below. By contrast, While the
523 cooler surface temperatures during the glacial period exerted a cooling effect on ice
524 sheet temperature, lower surface accumulation rate should have been lower during
525 glacial periods, which would have rates over the same period induced a warming
526 influence on ice sheet temperature effect. Uncertainties in bed topography should
527 influence both our thermal and our mechanical models, with deeper ice being more
528 likely to be warm, and with errors in ice thickness producing compensating errors in
529 basal sliding in our mechanical inversion. In the study of Huang et al. (2024),
530 BedMachine v2 was used for ice thickness and subglacial topography. However,
531 Bedmap3 (Pritchard et al., 2025) has better-resolved mountains and smoother trough
532 margins.

533 The simulation results we use from Huang et al. (2024) came from a 3D isotropic
534 full-Stokes ice flow model. While full-Stokes is generally considered the gold standard
535 of an ice sheet mechanical modeling model with the most complete physical processes
536 to date, the use of an isotropic rheology may not be valid in some parts of the ice sheet,

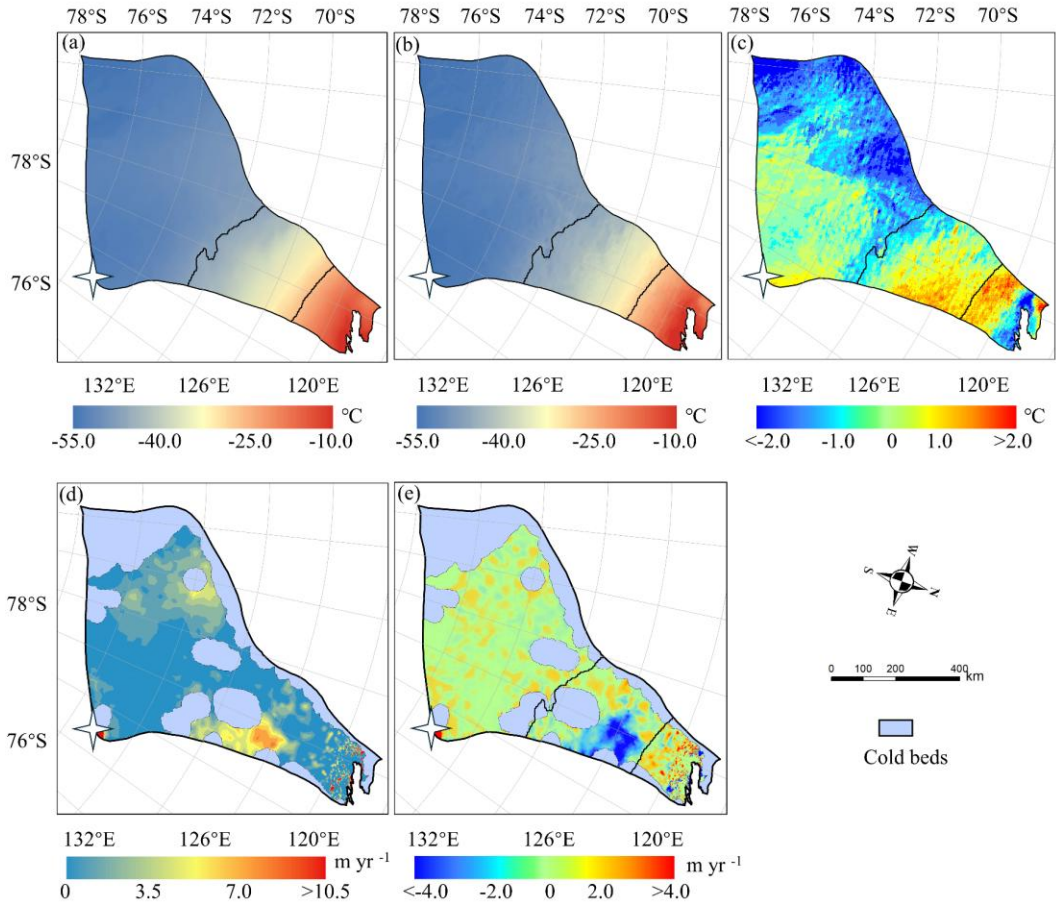
such as near ice divides or at the margin of an ice stream where the history of past ice deformation creates anisotropic crystal fabric that affects the present-day mechanical properties (Martín et al., 2009; Zhao et al., 2018b, 2018; Zwinger et al., 2014). Isotropic flow laws often require the use of an “enhancement factor” for vertical shear in the lower part of the ice column, an ad hoc correction that would have a particularly large influence on our computed overcooling metrics. Thus the isotropic flow law potentially introduces errors in modelled strain rates and, hence, bias in basal sliding velocities obtained by inversion methods (Budd and Jacka, 1989; Gerber et al., 2023; Rathmann and Lilien, 2022). Simulated surface ice velocities can be influenced by other factors in addition to ice fabric; shear margins are also impacted by accumulated rupture, such as damage along a shear margin (e.g., Benn et al., 2022; Lhermitte et al., 2020; Schoof, 2004; Sun et al., 2017). Ice deposited during the last glaciation has different chemistry (especially concentrations of chloride and possibly sulphate ions) which leads to smaller crystals that develop a strong, near-vertical, single-maximum fabric (Paterson, 1991). However, ice fabric data is sparse, known from direct observations at ice cores (Azuma and Higashi, 1985) or inferred from specialized radar measurements (Fujita and Mae, 1994; Jordan et al., 2022), and its impact is beyond the scope of this study as we refrain from incorporating additional observational data relying only on widely-available surface ice velocities.

Our inconsistency metrics are designed to provide bidirectional constraints, wherein the model is penalized for both overheating and overcooling. By adopting this bidirectional constraint framework, we aim to mitigate the risk of unidirectional constraints leading to excessively cold or warm outcomes being deemed optimal. However, our inconsistency metrics only provide a bidirectional constraint when viewed in a spatially integrated sense. Locally, we only have unidirectional constraints. This is because our overheating metrics are only computed where the bed is at the melting point, and our overcooling metrics are only computed where the bed is below the melting point. This makes methodological sense, as ~~we know for sure that~~ sliding must only ~~is~~ is generally expected to occur where the bed is thawed. However, in reality it is entirely possible that some of the areas where the modelled bed reaches the pressure melting point are still too cold (the modelled melt rate is lower than the real melt rate), and conversely, it is also possible that some of the areas where the modelled bed is below the pressure melting point are still too warm (the real temperature is colder still). Our method cannot identify these areas. Thus, our inconsistency metrics may underestimate variability in the ice sheet thermal state: we have no way to penalize frozen regions that are not cold enough or thawed regions that are not warm enough. We leave the development of these constraints to future work.

4.3 Impact of Input Datasets

576 There is a common area between 69°S and 72°S in the eastern part of Totten
577 Glacier with the largest AOH (Fig. 6) for all the GHFs varying from 48 to 70 mW m⁻²,
578 which suggests that the AOH inconsistency is from other ice sheet properties rather than
579 GHF. Zhang et al. (2022) reconstructed Antarctic near-surface air temperature based on
580 MODIS land surface temperature measurements and in situ air temperature records
581 from meteorological stations from 2001 to 2018. We compared the reconstruction of
582 near-surface air temperature in the year 2001 (Zhang et al., 2022) and the ALBMAP v1
583 dataset used in Huang et al. (2024). The surface air temperature in the area with large
584 AOH from ALBMAP v1 is 0.6-3.1 °C higher than that from the reconstructed near-
585 surface air temperature in 2001 (Fig. 9). The MODIS-based near-surface air
586 temperature product shows warming in Totten Glacier from 2001 to 2018. Even so, the
587 surface air temperature in the area with large AOH from ALBMAP v1 is still higher
588 than that in 2018 but over a smaller area. Therefore, we infer that the large AOH may
589 be attributed to a warm bias in the present-day ice surface temperature derived from
590 ALBMAP v1 in this area. The englacial temperature will be lower than present-day ice
591 sheet surface temperature used in the model but warmer than the average surface
592 temperature during the last glacial-interglacial cycle. We lowered the surface ice
593 temperature in this area by 1 °C, reran the simulation, and found that AOH with all the
594 GHFs was halved (Fig. 9e).

595



597 **4.23.1 Figure 9.** Surface ice temperature from ALBMAP v1 (a) and MODIS-based
 598 near-surface air temperature (b) in the year 2001, and their difference (c). (d) The
 599 AOH using modified surface ice temperature by reducing the temperature between
 600 the two black lines (contour lines of -44°C and -26°C) in (a) by 1°C and GHF
 601 of Martos et al. (2017). (e) The difference between the AOH using cooler surface
 602 ice temperature and the original AOH. **Sensitivity of Inconsistencies to GHF**
 603 **Datasets**

604 Comparing the GHF dataset rankings between this study and Huang et al. (2024),
 605 we find that the top 4 and the bottom 4 are the same in the two studies, albeit with slight
 606 variations in ranking. The lower ranking of Shen et al. (2020) in this study may be
 607 attributed to several factors. Firstly, Huang et al. (2024) excludes areas with ice speed
 608 exceeding 30 m a^{-1} (Fig. 4e) because specularity content is an ambiguous indicator of
 609 wet beds there. Secondly, the GHF from Shen et al. (2020) yields higher basal
 610 temperature and also faster basal ice velocities in most of the frozen bed of Totten
 611 Glacier, hence exhibits greater overcooling inconsistency, compared with Purucker et
 612 al. (2012), leading to a decrease in its rankings (Fig. S3). Lastly, Huang et al. (2024)

613 primarily relied on specularity content, while our study evaluated datasets based on
614 inconsistencies in the simulation results. Despite these methodological differences, both
615 studies identified four relatively well performing GHF datasets for Totten Glacier,
616 which exhibit similar distributions of thawed and frozen beds when compared to the
617 other four datasets (Fig. 4 and Fig. 6). This similarity underscores that the thawed bed
618 is concentrated near and upstream of the grounding line. Datasets from Stål et al. (2021),
619 Martos et al. (2017), Haeger et al. (2022), and Lösing and Ebbing (2021) exhibit a
620 tendency to overestimate GHF in central Totten Glacier.

621 Simulations employing GHF datasets from Stål et al. (2021), Martos et al. (2017),
622 Haeger et al. (2022), and Lösing and Ebbing (2021) yield more extensive thawed
623 bedded regions and are expected to exhibit greater overheating inconsistency.
624 Nevertheless, these models also exhibit relatively high overcooling inconsistency
625 despite the limited extent of frozen bedded regions. We quantified the discrepancies
626 between these four GHF datasets and the Purucker et al. (2012) GHF in terms of
627 modelled basal velocity, basal temperature relative to the pressure melting point, and
628 AOC (Fig. S5). The Purucker et al. (2012) GHF yields lower basal ice temperatures and
629 slower basal velocities across most frozen bedded regions, consequently resulting in
630 lower AOC values compared to the other four GHF datasets.

631

632 The white star represents Dome C.

633

634 **4.4 Implications for Ice Sheet Dynamics**

635 While evaluating inconsistencies highlights the spatial distribution of mismatches,
636 it does not inherently elucidate their underlying causes. The primary factors to
637 investigate are surface temperature, GHF, accumulation rate, and ice thickness,
638 representing the most critical boundary conditions. Furthermore, integrating multiple
639 sources of prior knowledge can help constrain model parameters:

- 640 1. High-resolution radar measurements: The availability of ice thickness data along
641 flight lines should be assessed to validate geometric boundary conditions.
- 642 2. Paleoclimate context: Historical climate reconstructions indicate significantly colder
643 surface temperatures during glacial periods compared to present-day conditions, with
644 correspondingly lower accumulation rates. These paleo-temperature conditions likely
645 induced a long-term thermal memory within the ice column, potentially contributing to
646 observed discrepancies between modeled and measured basal properties.

647 Therefore, we recommend a systematic evaluation of: (1) The spatial distribution
648 of radar-derived ice thickness measurements; (2) The temporal consistency of surface
649 temperature boundary conditions; (3) The sensitivity of model results to GHF variations;
650 (4) Accumulation rate reconstructions during key climatic periods. This multi-faceted
651 approach helps isolate the causes of inconsistencies in ice sheet simulations.

652 There is a common area between 69°S and 72°S in the eastern part of Totten
653 Glacier with the largest AOH (Fig. 6) for all the GHFs varying from 48 to 70 mW m^{-2} ,
654 which suggests that the AOH inconsistency is from other ice sheet properties rather than
655 GHF. Zhang et al. (2022) reconstructed Antarctic near surface air temperature based on
656 MODIS land surface temperature measurements and in situ air temperature records
657 from meteorological stations from 2001 to 2018. We compared the reconstruction of
658 near surface air temperature in the year 2001 (Zhang et al., 2022) and the ALBMAP v1
659 dataset used in Huang et al. (2024). The surface air temperature in the area with large
660 AOH from ALBMAP v1 is 0.6–3.1 °C higher than that from the reconstructed near
661 surface air temperature in 2001 (Fig. 9). The MODIS based near surface air
662 temperature product shows warming in Totten Glacier from 2001 to 2018. Even so, the
663 surface air temperature in the area with large AOH from ALBMAP v1 is still higher
664 than that in 2018 but over a smaller area. Therefore, we infer that the large AOH may
665 be attributed to the present-day ice surface temperature derived from ALBMAP v1 in
666 this area being unrealistically warm. The englacial temperature will be lower than
667 present-day ice sheet surface temperature used in the model but warmer than the
668 average surface temperature during the last glacial interglacial cycle. We lowered the
669 surface ice temperature in this area by 1 °C, reran the simulation, and found that AOH
670 with all the GHFs was halved (Fig. 9e).

671

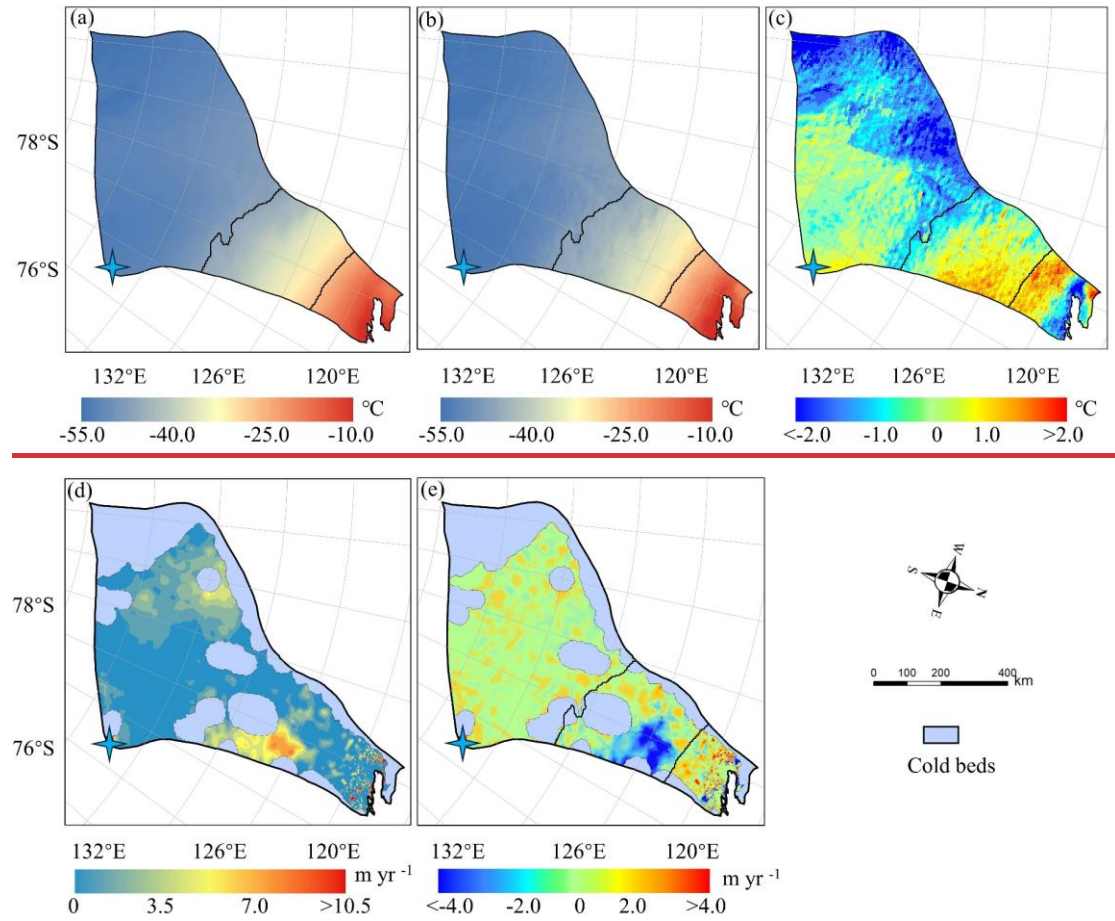


Figure 9. Surface ice temperature from ALBMAP v1 (a) and MODIS-based near-surface air temperature (b) in the year 2001, and their difference (c). (d) The AOH using modified surface ice temperature by reducing the temperature between the two thick black curves (contour lines of -44°C and -26°C) in (a) by 1°C and GHF of Martos et al. (2017). (e) The difference between the AOH using cooler surface ice temperature and the original AOH. The blue star represents Dome C.

Given that data assimilation and inverse methods are widely employed to infer basal friction coefficients in ice sheet simulations, it is essential to acknowledge the impact of the inconsistencies identified in our study on ice sheet dynamics. A frozen bed is supposed to provide substantial resistance and limit basal sliding; however, if the basal temperature is overestimated, it may decrease viscosity and enhance basal sliding. This overheating inconsistency would lead to an overestimation of ice flow speeds, discharge, and the dynamic ice loss (Artemieva, 2022; Burton-Johnson et al., 2020). Similarly, underrepresentation of thawed bedding would slow bed conditions will lead to an underestimation of ice discharge estimates, and hence potential, consequently, an underestimation of ice sheet's response to climate warming.

689 The basal thermal regime critically influences the stability of grounding lines and the
690 behavior of ice streams-[\(Dawson et al., 2022; Robel et al., 2014\)](#). In a warming climate,
691 increases in geothermal or frictional heating can trigger basal thawing in these areas,
692 lowering basal friction and potentially initiating rapid grounding line retreat—a key
693 component of marine ice sheet instability (MISI) (Reese et al., 2023; Ross et al., 2012).
694 Without incorporating a self-consistent thermal model into the inversion, projections
695 may misrepresent the onset and extent of these dynamic instabilities. Our findings
696 underscore that a fully coupled inversion framework would use not only surface
697 velocity data but also incorporate direct or proxy observations of basal temperature and
698 subglacial hydrology. Such an approach would better constrain the basal friction
699 coefficient in a physically consistent manner, reducing the risk of producing
700 nonphysical states. This integration is especially critical for projections of ice sheet
701 evolution under [future](#) climate change [scenarios](#), as the dynamic response is sensitive
702 to even small changes in basal conditions.

704 5. Conclusion

705 We propose a novel and rapid method to quantify the inconsistencies between
706 modelled basal ice temperature and observed surface [ice speed](#)[velocity](#)[magnitude](#) and
707 assess the quality of ice sheet model simulation results without using subglacial
708 observation data. Previously, it has been assumed that [ehecking](#)[assessing](#) the quality of
709 an ice sheet temperature model required in situ observations, whether from ice cores or
710 geophysical techniques like ice penetrating radar. By using the ice temperature field to
711 compute the rheology structure needed for a mechanical inversion and then quantifying
712 the inconsistency between the inverted velocity field and the original ice temperature
713 field, we are able to use remotely sensed surface velocity observations as a [eheck](#)[means](#)
714 [to assess](#) on the quality of modelled [englacial](#)[basal](#) temperatures. Given the challenges
715 in acquiring subglacial data, our method can provide a streamlined and effective
716 approach to evaluation.

717 We apply this method to [evaluate](#) the [steady-state](#) simulation results of Totten
718 Glacier [presented by Huang et al. \(2024\)](#), which were derived using a 3D full-Stokes
719 model with 8 different GHF datasets. Assuming the inconsistencies are mainly due to
720 [unrealistic](#)[quality](#) [issues](#) [of](#) GHF datasets, we use the inconsistencies to assess the
721 reliability of those GHF datasets. We compare our GHF ranking with that by Huang et
722 al. (2024) which used specularity content to derive a two-sided constraint on the basal
723 thermal state. We find that the top 4 and the bottom 4 GHFs are the same in the two
724 studies, albeit with slight variations in ranking. Furthermore, we find that the
725 simulations with all GHF datasets underestimate the basal ice temperature in a canyon
726 on the western boundary of Totten Glacier, and we infer that the common high
727 overheating inconsistencies with all the GHF datasets in the eastern Totten Glacier

728 between 69°S and 72°S may be attributed to ~~the unrealistically a~~ warm bias in the
729 prescribed surface ice temperature used ~~there~~ in the model. While we demonstrate that
730 this approach works on simulation results for Totten Glacier, testing of the method on
731 other glaciers would be useful to assess if the approach is worthwhile for revealing
732 ambiguous conflicts in observations and simulations.

733

734

735

736 *Data availability.* MEaSURES BedMachine Antarctica, version 2, is available at
737 <https://doi.org/10.5067/E1QL9HFQ7A8M> (Morlighem, 2020). MEaSURES InSAR-
738 Based Antarctic Ice Velocity Map, version 2, is available at
739 <https://doi.org/10.5067/D7GK8F5J8M8R> (Rignot et al., 2017). MEaSURES Antarctic
740 Boundaries for IPY 2007–2009 from Satellite Radar, version 2, is available at
741 <https://doi.org/10.5067/AXE4121732AD> (Mouginot et al., 2017). ALBMAP v1 and the
742 GHF dataset of Shapiro and Ritzwoller (2004) are available at
743 <https://doi.org/10.1594/PANGAEA.734145> (Le Brocq et al., ~~2010b~~²⁰¹⁰). The GHF
744 dataset of An et al. (2015) is available at
745 <http://www.seismolab.org/model/antarctica/lithosphere/AN1-HF.tar.gz> (last access: 11
746 April 2023). The GHF dataset of Shen et al. (2020) is available at
747 <https://sites.google.com/view/weisen/research-products?authuser=0> (last access: 11
748 April 2023). The GHF dataset of Martos (2017) is available at
749 <https://doi.org/10.1594/PANGAEA.882503>. The GHF dataset of Purucker (2012) is
750 available
751 https://core2.gsfc.nasa.gov/research/purucker/heatflux_mf7_foxmaule05.txt (last
752 access: 11 April 2023).

753

754 *Author contributions.* LZ and JCM conceived the study. LZ, MW, and JCM designed
755 the methodology. JW and LZ analyzed the data and conducted visualization. JW
756 and LZ wrote the original draft, and all the authors revised the paper.

757

758 *Competing interests.* The contact author has declared that none of the authors has any
759 competing interests.

760

761 *Acknowledgements.* This work was supported by National Natural Science Foundation
762 of China (grant no. 42576280) and Academy of Finland (grant no. 355572).

763

764 **References**

765 Albrecht, T., Winkelmann, R., and Levermann, A.: Glacial-cycle simulations of the Antarctic Ice
766 Sheet with the Parallel Ice Sheet Model (PISM) – Part 1: Boundary conditions and climatic
767 forcing, *The Cryosphere*, 14, 599–632, <https://doi.org/10.5194/tc-14-599-2020>, 2020.

768 An, M., Wiens, D. A., Zhao, Y., Feng, M., Nyblade, A., Kanao, M., Li, Y., Maggi, A., and Lévêque,
769 J.: Temperature, lithosphere-asthenosphere boundary, and heat flux beneath the Antarctic Plate
770 inferred from seismic velocities, *J. Geophys. Res. Solid Earth*, 120, 8720–8742,
771 <https://doi.org/10.1002/2015JB011917>, 2015.

772 Artemieva, I. M.: Antarctica ice sheet basal melting enhanced by high mantle heat, *Earth-Sci. Rev.*,
773 226, 103954, <https://doi.org/10.1016/j.earscirev.2022.103954>, 2022.

774 Azuma, N. and Higashi, A.: Formation Processes of Ice Fabric Pattern in Ice Sheets, *Ann. Glaciol.*,
775 6, 130–134, <https://doi.org/10.3189/1985AoG6-1-130-134>, 1985.

776 Benn, D. I., Luckman, A., Åström, J. A., Crawford, A. J., Cornford, S. L., Bevan, S. L., Zwinger, T.,
777 Gladstone, R., Alley, K., Pettit, E., and Bassis, J.: Rapid fragmentation of Thwaites Eastern Ice
778 Shelf, *The Cryosphere*, 16, 2545–2564, <https://doi.org/10.5194/tc-16-2545-2022>, 2022.

779 Brondex, J., Gagliardini, O., Gillet-Chaulet, F., and Durand, G.: Sensitivity of grounding line
780 dynamics to the choice of the friction law, *J. Glaciol.*, 63, 854–866,
781 <https://doi.org/10.1017/jog.2017.51>, 2017.

782 Brondex, J., Gillet-Chaulet, F., and Gagliardini, O.: Sensitivity of centennial mass loss projections
783 of the Amundsen basin to the friction law, *The Cryosphere*, 13, 177–195,
784 <https://doi.org/10.5194/tc-13-177-2019>, 2019.

785 Budd, W. F. and Jacka, T. H.: A review of ice rheology for ice sheet modelling, *Cold Reg. Sci.
786 Technol.*, 16, 107–144, [https://doi.org/10.1016/0165-232X\(89\)90014-1](https://doi.org/10.1016/0165-232X(89)90014-1), 1989.

787 Budd, W. F., Keage, P. L., and Blundy, N. A.: Empirical Studies of Ice Sliding, *J. Glaciol.*, 23, 157–
788 170, <https://doi.org/10.3189/S0022143000029804>, 1979.

789 Burton-Johnson, A., Dziadek, R., and Martin, C.: Review article: Geothermal heat flow in
790 Antarctica: current and future directions, *The Cryosphere*, 14, 3843–3873,
791 <https://doi.org/10.5194/tc-14-3843-2020>, 2020.

792 Choi, Y., Seroussi, H., Morlighem, M., Schlegel, N.-J., and Gardner, A.: Impact of time-dependent
793 data assimilation on ice flow model initialization and projections: a case study of Kjer Glacier,
794 Greenland, *The Cryosphere*, 17, 5499–5517, <https://doi.org/10.5194/tc-17-5499-2023>, 2023.

795 Cornford, S. L., Martin, D. F., Payne, A. J., Ng, E. G., Le Brocq, A. M., Gladstone, R. M., Edwards,
796 T. L., Shannon, S. R., Agosta, C., Van Den Broeke, M. R., Hellmer, H. H., Krinner, G.,
797 Ligtenberg, S. R. M., Timmermann, R., and Vaughan, D. G.: Century-scale simulations of the
798 response of the West Antarctic Ice Sheet to a warming climate, *The Cryosphere*, 9, 1579–1600,
799 <https://doi.org/10.5194/tc-9-1579-2015>, 2015.

800 [Dawson, E. J., Schroeder, D. M., Chu, W., Mantelli, E., and Seroussi, H.: Ice mass loss sensitivity
801 to the Antarctic ice sheet basal thermal state, *Nat. Commun.*, 13, 4957,
802 <https://doi.org/10.1038/s41467-022-32632-2>, 2022.](#)

803 [Dow, C.: Aurora Subglacial Basin GlaDs inputs, outputs and geophysical data, Zenodo \[data set\],
804 <https://doi.org/10.5281/zenodo.3525474>, 2019.](#)

805 Dow, C. F., McCormack, F. S., Young, D. A., Greenbaum, J. S., Roberts, J. L., and Blankenship, D.
806 D.: Totten Glacier subglacial hydrology determined from geophysics and modeling, *Earth
807 Planet. Sci. Lett.*, 531, 115961, <https://doi.org/10.1016/j.epsl.2019.115961>, 2020.

808 Dziadek, R., Gohl, K., Diehl, A., and Kaul, N.: Geothermal heat flux in the Amundsen Sea sector
809 of West Antarctica: New insights from temperature measurements, depth to the bottom of the
810 magnetic source estimation, and thermal modeling, *Geochem. Geophys. Geosystems*, 18,
811 2657–2672, <https://doi.org/10.1002/2016GC006755>, 2017.

812 Fisher, A. T., Mankoff, K. D., Tulaczyk, S. M., Tyler, S. W., and Foley, N.: High geothermal heat
813 flux measured below the West Antarctic Ice Sheet, *Sci. Adv.*, 1(6), e1500093,
814 <https://doi.org/10.1126/sciadv.1500093>, 2015.

815 Fowler, A. C.: A theoretical treatment of the sliding of glaciers in the absense of cavitation, *Philos.*
816 *Trans. R. Soc. Lond. Ser. Math. Phys. Sci.*, 298, 637–681,
817 <https://doi.org/10.1098/rsta.1981.0003>, 1981.

818 Fujita, S. and Mae, S.: Strain in the ice sheet deduced from the crystal-orientation fabrics from bare
819 icefields adjacent to the Sør-Rondane Mountains, Dronning Maud Land, East Antarctica, *J.*
820 *Glaciol.*, 40, 135–139, <https://doi.org/10.3189/S002214300003907>, 1994.

821 Gagliardini, O., Cohen, D., Råback, P., and Zwinger, T.: Finite-element modeling of subglacial
822 cavities and related friction law, *J. Geophys. Res. Earth Surf.*, 112, F02027,
823 <https://doi.org/10.1029/2006JF000576>, 2007.

824 Gerber, T. A., Lilien, D. A., Rathmann, N. M., Franke, S., Young, T. J., Valero-Delgado, F., Ershadi,
825 M. R., Drews, R., Zeising, O., Humbert, A., Stoll, N., Weikusat, I., Grinsted, A., Hvidberg, C.
826 S., Jansen, D., Miller, H., Helm, V., Steinhage, D., O'Neill, C., Paden, J., Gogineni, S. P., Dahl-
827 JENSEN, D., and Eisen, O.: Crystal orientation fabric anisotropy causes directional hardening of
828 the Northeast Greenland Ice Stream, *Nat. Commun.*, 14, 2653, <https://doi.org/10.1038/s41467-023-38139-8>, 2023.

829 Gillet-Chaulet, F., Gagliardini, O., Seddik, H., Nodet, M., Durand, G., Ritz, C., Zwinger, T., Greve,
830 R., and Vaughan, D. G.: Greenland ice sheet contribution to sea-level rise from a new-
831 generation ice-sheet model, *The Cryosphere*, 6, 1561–1576, <https://doi.org/10.5194/tc-6-1561-2012>, 2012.

832 Gladstone, R., Schäfer, M., Zwinger, T., Gong, Y., Strozzi, T., Mottram, R., Boberg, F., and Moore,
833 J. C.: Importance of basal processes in simulations of a surging Svalbard outlet glacier, *The*
834 *Cryosphere*, 8, 1393–1405, <https://doi.org/10.5194/tc-8-1393-2014>, 2014.

835 Greenbaum, J. S., Blankenship, D. D., Young, D. A., Richter, T. G., Roberts, J. L., Aitken, A. R. A.,
836 Legresy, B., Schroeder, D. M., Warner, R. C., van Ommen, T. D., and Siegert, M. J.: Ocean
837 access to a cavity beneath Totten Glacier in East Antarctica, *Nat. Geosci.*, 8, 294–298,
838 <https://doi.org/10.1038/ngeo2388>, 2015.

839 Haeger, C., Petrunin, A. G., and Kaban, M. K.: Geothermal Heat Flow and Thermal Structure of the
840 Antarctic Lithosphere, *Geochem. Geophys. Geosystems*, 23, e2022GC010501,
841 <https://doi.org/10.1029/2022GC010501>, 2022.

842 Huang, Y., Zhao, L., Wolovick, M., Ma, Y., and Moore, J. C.: Using specularity content to evaluate
843 eight geothermal heat flow maps of Totten Glacier, *The Cryosphere*, 18, 103–119,
844 <https://doi.org/10.5194/tc-18-103-2024>, 2024.

845 Jordan, T. M., Martín, C., Brisbourne, A. M., Schroeder, D. M., and Smith, A. M.: Radar
846

848 Characterization of Ice Crystal Orientation Fabric and Anisotropic Viscosity Within an
849 Antarctic Ice Stream, *J. Geophys. Res. Earth Surf.*, 127, e2022JF006673,
850 <https://doi.org/10.1029/2022JF006673>, 2022.

851 Kamb, B.: Sliding motion of glaciers: Theory and observation, *Rev. Geophys.*, 8, 673–728,
852 <https://doi.org/10.1029/RG008i004p00673>, 1970.

853 Kang, H., Zhao, L., Wolovick, M., and Moore, J. C.: Evaluation of six geothermal heat flux maps
854 for the Antarctic Lambert–Amery glacial system, *The Cryosphere*, 16, 3619–3633,
855 <https://doi.org/10.5194/tc-16-3619-2022>, 2022.

856 Kim, B.-H., Seo, K.-W., Lee, C.-K., Kim, J.-S., Lee, W. S., Jin, E. K., and Van Den Broeke, M.:
857 Partitioning the drivers of Antarctic glacier mass balance (2003–2020) using satellite
858 observations and a regional climate model, *Proc. Natl. Acad. Sci.*, 121, e2322622121,
859 <https://doi.org/10.1073/pnas.2322622121>, 2024.

860 Larour, E., Seroussi, H., Morlighem, M., and Rignot, E.: Continental scale, high order, high spatial
861 resolution, ice sheet modeling using the Ice Sheet System Model (ISSM), *J. Geophys. Res.*,
862 117, F01022, <https://doi.org/10.1029/2011JF002140>, 2012.

863 Le Brocq, A. M., Payne, A. J., and Vieli, A.: An improved Antarctic dataset for high resolution
864 numerical ice sheet models (ALBMAP v1), *Earth Syst. Sci. Data*, 2, 247–260,
865 <https://doi.org/10.5194/essd-2-247-2010>, 2010.

866 Lipscomb, W. H., Leguy, G. R., Jourdain, N. C., Asay-Davis, X., Seroussi, H., and Nowicki, S.:
867 ISMIP6-based projections of ocean-forced Antarctic Ice Sheet evolution using the
868 Community Ice Sheet Model, *The Cryosphere*, 15, 633–661, <https://doi.org/10.5194/tc-15-633-2021>, 2021.

869 Lhermitte, S., Sun, S., Shuman, C., Wouters, B., Pattyn, F., Wuire, J., Berthier, E., and Nagler, T.:
870 Damage accelerates ice shelf instability and mass loss in Amundsen Sea Embayment, *Proc.
871 Natl. Acad. Sci.*, 117, 24735–24741, <https://doi.org/10.1073/pnas.1912890117>, 2020.

872 Lösing, M. and Ebbing, J.: Predicting Geothermal Heat Flow in Antarctica With a Machine Learning
873 Approach, *J. Geophys. Res. Solid Earth*, 126, e2020JB021499,
874 <https://doi.org/10.1029/2020JB021499>, 2021.

875 MacAyeal, D. R.: A tutorial on the use of control methods in ice-sheet modeling, *J. Glaciol.*, 39, 91–
876 98, <https://doi.org/10.3189/S0022143000015744>, 1993.

877 Martín, C., Gudmundsson, G. H., Pritchard, H. D., and Gagliardini, O.: On the effects of anisotropic
878 rheology on ice flow, internal structure, and the age-depth relationship at ice divides, *J.
879 Geophys. Res. Earth Surf.*, 114, F04001, <https://doi.org/10.1029/2008JF001204>, 2009.

880 Martos, Y. M., Catalán, M., Jordan, T. A., Golynsky, A., Golynsky, D., Eagles, G., and Vaughan, D.
881 G.: Heat Flux Distribution of Antarctica Unveiled, *Geophys. Res. Lett.*, 44, 11,417–11,426,
882 <https://doi.org/10.1002/2017GL075609>, 2017.

883 Maule, C. F., Purucker, M. E., Olsen, N., and Mosegaard, K.: Heat Flux Anomalies in Antarctica
884 Revealed by Satellite Magnetic Data, *Science*, 309, 464–467,
885 <https://doi.org/10.1126/science.1106888>, 2005.

886 McCormack, F. S., Roberts, J. L., Dow, C. F., Stål, T., Halpin, J. A., Reading, A. M., and Siegert, M.

888 J.: Fine-Scale Geothermal Heat Flow in Antarctica Can Increase Simulated Subglacial Melt
889 Estimates, *Geophys. Res. Lett.*, 49, e2022GL098539, <https://doi.org/10.1029/2022GL098539>,
890 2022.

891 Morlighem, M., Seroussi, H., Larour, E., and Rignot, E.: Inversion of basal friction in Antarctica
892 using exact and incomplete adjoints of a higher-order model, *J. Geophys. Res. Earth Surf.*, 118,
893 1746–1753, <https://doi.org/10.1002/jgrf.20125>, 2013.

894 Morlighem, M., Rignot, E., Binder, T., Blankenship, D., Drews, R., Eagles, G., Eisen, O., Ferraccioli,
895 F., Forsberg, R., Fretwell, P., Goel, V., Greenbaum, J. S., Gudmundsson, H., Guo, J., Helm, V.,
896 Hofstede, C., Howat, I., Humbert, A., Jokat, W., Karlsson, N. B., Lee, W. S., Matsuoka, K.,
897 Millan, R., Mouginot, J., Paden, J., Pattyn, F., Roberts, J., Rosier, S., Ruppel, A., Seroussi, H.,
898 Smith, E. C., Steinhage, D., Sun, B., Broeke, M. R. V. D., Ommen, T. D. V., Wessem, M. V.,
899 and Young, D. A.: Deep glacial troughs and stabilizing ridges unveiled beneath the margins of
900 the Antarctic ice sheet, *Nat. Geosci.*, 13, 132–137, <https://doi.org/10.1038/s41561-019-0510-8>, 2020.

901 Nye, J. F.: Glacier sliding without cavitation in a linear viscous approximation, *Proc. R. Soc. Lond.*
902 *Math. Phys. Sci.*, 315, 381–403, <https://doi.org/10.1098/rspa.1970.0050>, 1970.

903 Park, I.-W., Jin, E. K., Morlighem, M., and Lee, K.-K.: Impact of boundary conditions on the
904 modeled thermal regime of the Antarctic ice sheet, *The Cryosphere*, 18, 1139–1155,
905 <https://doi.org/10.5194/tc-18-1139-2024>, 2024.

906 Paterson, W. S. B.: Why ice-age ice is sometimes “soft,” *Cold Reg. Sci. Technol.*, 20, 75–98,
907 [https://doi.org/10.1016/0165-232X\(91\)90058-O](https://doi.org/10.1016/0165-232X(91)90058-O), 1991.

908 Pattyn, F.: Sea-level response to melting of Antarctic ice shelves on multi-centennial timescales
909 with the fast Elementary Thermomechanical Ice Sheet model (f.ETISh v1.0), *The*
910 *Cryosphere*, 11, 1851–1878, <https://doi.org/10.5194/tc-11-1851-2017>, 2017.

911 Payne, A. J., Nowicki, S., Abe-Ouchi, A., Agosta, C., Alexander, P., Albrecht, T., Asay-Davis, X.,
912 Aschwanden, A., Barthel, A., Bracegirdle, T. J., Calov, R., Chambers, C., Choi, Y., Cullather,
913 R., Cuzzone, J., Dumas, C., Edwards, T. L., Felikson, D., Fettweis, X., Galton-Fenzi, B. K.,
914 Goelzer, H., Gladstone, R., Golledge, N. R., Gregory, J. M., Greve, R., Hattermann, T.,
915 Hoffman, M. J., Humbert, A., Huybrechts, P., Jourdain, N. C., Kleiner, T., Munneke, P. K.,
916 Larour, E., Le Clec'H, S., Lee, V., Leguy, G., Lipscomb, W. H., Little, C. M., Lowry, D. P.,
917 Morlighem, M., Nias, I., Pattyn, F., Pelle, T., Price, S. F., Quiquet, A., Reese, R., Rückamp, M.,
918 Schlegel, N., Seroussi, H., Shepherd, A., Simon, E., Slater, D., Smith, R. S., Straneo, F., Sun,
919 S., Tarasov, L., Trusel, L. D., Van Breedam, J., Van De Wal, R., Van Den Broeke, M.,
920 Winkelmann, R., Zhao, C., Zhang, T., and Zwinger, T.: Future Sea Level Change Under
921 Coupled Model Intercomparison Project Phase 5 and Phase 6 Scenarios From the Greenland
922 and Antarctic Ice Sheets, *Geophys. Res. Lett.*, 48, e2020GL091741,
923 <https://doi.org/10.1029/2020GL091741>, 2021.

924 Peyaud, V., Bouchayer, C., Gagliardini, O., Vincent, C., Gillet-Chaulet, F., Six, D., and Laarman,
925 O.: Numerical modeling of the dynamics of the Mer de Glace glacier, French Alps: comparison
926 with past observations and forecasting of near-future evolution, *The Cryosphere*, 14, 3979–

928 3994, <https://doi.org/10.5194/tc-14-3979-2020>, 2020.

929 Pittard, M. L., Roberts, J. L., Galton-Fenzi, B. K., and Watson, C. S.: Sensitivity of the Lambert-
930 Amery glacial system to geothermal heat flux, *Ann. Glaciol.*, 57, 56 – 68,
931 <https://doi.org/10.1017/aog.2016.26>, 2016.

932 Pollard, D. and DeConto, R. M.: A simple inverse method for the distribution of basal sliding
933 coefficients under ice sheets, applied to Antarctica, *The Cryosphere*, 6, 953–971,
934 <https://doi.org/10.5194/tc-6-953-2012>, 2012.

935 Pritchard, H. D., Arthern, R. J., Vaughan, D. G., and Edwards, L. A.: Extensive dynamic thinning
936 on the margins of the Greenland and Antarctic ice sheets, *Nature*, 461, 971–975,
937 <https://doi.org/10.1038/nature08471>, 2009.

938 Pritchard, H.D., Fretwell, P.T., Freymond, A.C. et al. Bedmap3 updated ice bed, surface and thickness
939 gridded datasets for Antarctica. *Sci Data* 12, 414 (2025). <https://doi.org/10.1038/s41597-025-04672-y>

940 Purucker, M.: Geothermal heat flux data set based on low resolution observations collected by the
941 CHAMP satellite between 2000 and 2010, and produced from the MF-6 model following the
942 technique described in Fox Maule et al. (2005), Interactive System for Ice sheet Simulation
943 [data set], https://core2.gsfc.nasa.gov/research/purucker/heatflux_mf7_foxmaule05.txt (last
944 access: 24 December 2023), 2012.

945 Rathmann, N. M. and Lilien, D. A.: Inferred basal friction and mass flux affected by crystal-
946 orientation fabrics, *J. Glaciol.*, 68, 236–252, <https://doi.org/10.1017/jog.2021.88>, 2022.

947 Reading, A. M.: Antarctic geothermal heat flow and its implications for tectonics and ice sheets,
948 *Nat. Rev. Earth Environ.*, 3, 814–831, <https://doi.org/10.1038/s43017-022-00348-y>, 2022.

949 Reese, R., Garbe, J., Hill, E. A., Urruty, B., Naughten, K. A., Gagliardini, O., Durand, G., Gillet-
950 Chaulet, F., Gudmundsson, G. H., Chandler, D., Langebroek, P. M., and Winkelmann, R.: The
951 stability of present-day Antarctic grounding lines – Part 2: Onset of irreversible retreat of
952 Amundsen Sea glaciers under current climate on centennial timescales cannot be excluded,
953 *The Cryosphere*, 17, 3761–3783, <https://doi.org/10.5194/tc-17-3761-2023>, 2023.

954 Ross, N., Bingham, R. G., Corr, H. F. J., Ferraccioli, F., Jordan, T. A., Le Brocq, A., Rippin, D. M.,
955 Young, D., Blankenship, D. D., and Siegert, M. J.: Steep reverse bed slope at the grounding
956 line of the Weddell Sea sector in West Antarctica, *Nat. Geosci.*, 5, 393–396,
957 <https://doi.org/10.1038/ngeo1468>, 2012.

958 Robel, A. A., Schoof, C., and Tziperman, E.: Rapid grounding line migration induced by internal
959 ice stream variability, *J. Geophys. Res. Earth Surf.*, 119, 2430 – 2447,
960 <https://doi.org/10.1002/2014JF003251>, 2014.

961 Rignot, E., Mouginot, J., and Scheuchl, B.: MEaSUREs InSAR-Based Antarctica Ice Velocity Map,
962 Version 2, Boulder, Colorado USA, NASA National Snow and Ice Data Center Distributed
963 Active Archive Center [data Set], <https://doi.org/10.5067/D7GK8F5J8M8R>, 2017.

964 Rignot, E., Mouginot, J., Scheuchl, B., Van Den Broeke, M., Van Wessem, M. J., and Morlighem,
965 M.: Four decades of Antarctic Ice Sheet mass balance from 1979–2017, *Proc. Natl. Acad. Sci.*,
966 116, 1095–1103, <https://doi.org/10.1073/pnas.1812883116>, 2019.

968 Schannwell, C., Drews, R., Ehlers, T. A., Eisen, O., Mayer, C., Malinen, M., Smith, E. C., and
969 Eisermann, H.: Quantifying the effect of ocean bed properties on ice sheet geometry over 40
970 000 years with a full-Stokes model, *The Cryosphere*, 14, 3917–3934,
971 <https://doi.org/10.5194/tc-14-3917-2020>, 2020.

972 Schoof, C.: On the mechanics of ice-stream shear margins, *J. Glaciol.*, 50, 208–218,
973 <https://doi.org/10.3189/172756504781830024>, 2004.

974 Schoof, C.: The effect of cavitation on glacier sliding, *Proc. R. Soc. Math. Phys. Eng. Sci.*, 461,
975 609–627, <https://doi.org/10.1098/rspa.2004.1350>, 2005.

976 Schroeder, D. M., Blankenship, D. D., and Young, D. A.: Evidence for a water system transition
977 beneath Thwaites Glacier, West Antarctica, *Proc. Natl. Acad. Sci.*, 110, 12225–12228,
978 <https://doi.org/10.1073/pnas.1302828110>, 2013.

979 ~~Schroeder, D. M., Blankenship, D. D., Raney, R. K., and Grima, C.: Estimating Subglacial Water
980 Geometry Using Radar Bed Echo Specularity: Application to Thwaites Glacier, West
981 Antarctica, IEEE Geosci. Remote Sens. Lett., 12, 443–447,
982 <https://doi.org/10.1109/LGRS.2014.2337878>, 2015.~~

983 Seroussi, H., Nowicki, S., Simon, E., Abe-Ouchi, A., Albrecht, T., Brondex, J., Cornford, S., Dumas,
984 C., Gillet-Chaulet, F., Goelzer, H., Golledge, N. R., Gregory, J. M., Greve, R., Hoffman, M. J.,
985 Humbert, A., Huybrechts, P., Kleiner, T., Larour, E., Leguy, G., Lipscomb, W. H., Lowry, D.,
986 Mengel, M., Morlighem, M., Pattyn, F., Payne, A. J., Pollard, D., Price, S. F., Quiquet, A.,
987 Reerink, T. J., Reese, R., Rodehacke, C. B., Schlegel, N.-J., Shepherd, A., Sun, S., Sutter, J.,
988 Van Breedam, J., Van De Wal, R. S. W., Winkelmann, R., and Zhang, T.: initMIP-Antarctica:
989 an ice sheet model initialization experiment of ISMIP6, *The Cryosphere*, 13, 1441–1471,
990 <https://doi.org/10.5194/tc-13-1441-2019>, 2019.

991 Shackleton, C., Matsuoka, K., Moholdt, G., Van Liefferinge, B., and Paden, J.: Stochastic
992 Simulations of Bed Topography Constrain Geothermal Heat Flow and Subglacial Drainage
993 Near Dome Fuji, East Antarctica, *J. Geophys. Res. Earth Surf.*, 128, e2023JF007269,
994 <https://doi.org/10.1029/2023JF007269>, 2023.

995 Shapiro, N.: Inferring surface heat flux distributions guided by a global seismic model: particular
996 application to Antarctica, *Earth Planet. Sci. Lett.*, 223, 213–224,
997 <https://doi.org/10.1016/j.epsl.2004.04.011>, 2004.

998 Shen, W., Wiens, D. A., Lloyd, A. J., and Nyblade, A. A.: A Geothermal Heat Flux Map of Antarctica
999 Empirically Constrained by Seismic Structure, *Geophys. Res. Lett.*, 47, e2020GL086955,
1000 <https://doi.org/10.1029/2020GL086955>, 2020.

1001 Siahaan, A., Smith, R. S., Holland, P. R., Jenkins, A., Gregory, J. M., Lee, V., Mathiot, P., Payne, A.
1002 J., Ridley, J. K., and Jones, C. G.: The Antarctic contribution to 21st-century sea-level rise
1003 predicted by the UK Earth System Model with an interactive ice sheet, *The Cryosphere*, 16,
1004 4053 – 4086, <https://doi.org/10.5194/tc-16-4053-2022>, 2022.

1005 Smith-Johnsen, S., Schlegel, N. -J., De Fleurian, B., and Nisancioglu, K. H.: Sensitivity of the
1006 Northeast Greenland Ice Stream to Geothermal Heat, *J. Geophys. Res. Earth Surf.*, 125,
1007 e2019JF005252, <https://doi.org/10.1029/2019JF005252>, 2020.

1008 Stål, T., Reading, A. M., Halpin, J. A., and Whittaker, J. M.: Antarctic Geothermal Heat Flow Model:
1009 Aq1, Geochem. Geophys. Geosystems, 22, e2020GC009428,
1010 <https://doi.org/10.1029/2020GC009428>, 2021.

1011 Sun, S., Cornford, S. L., Moore, J. C., Gladstone, R., and Zhao, L.: Ice shelf fracture
1012 parameterization in an ice sheet model, The Cryosphere, 11, 2543–2554,
1013 <https://doi.org/10.5194/tc-11-2543-2017>, 2017.

1014 Tsai, V. C., Stewart, A. L., and Thompson, A. F.: Marine ice-sheet profiles and stability under
1015 Coulomb basal conditions, J. Glaciol., 61, 205–215, <https://doi.org/10.3189/2015JoG14J221>,
1016 2015.

1017 Van Liefferinge, B., Pattyn, F., Cavitte, M. G. P., Karlsson, N. B., Young, D. A., Sutter, J., and Eisen,
1018 O.: Promising Oldest Ice sites in East Antarctica based on thermodynamical modelling, The
1019 Cryosphere, 12, 2773–2787, <https://doi.org/10.5194/tc-12-2773-2018>, 2018.

1020 Weertman, J.: On the Sliding of Glaciers, J. Glaciol., 3, 33–38,
1021 <https://doi.org/10.3189/S0022143000024709>, 1957.

1022 Young, D. A., Schroeder, D. M., Blankenship, D. D., Kempf, S. D., and Quartini, E.: The distribution
1023 of basal water between Antarctic subglacial lakes from radar sounding, Philos. Trans. R. Soc.
1024 Math. Phys. Eng. Sci., 374, 20140297, <https://doi.org/10.1098/rsta.2014.0297>, 2016.

1025 Zhao, L., Moore, J. C., Gladstone, R. M., Warner, R. C., King, M. A., Zwinger, TSun, B., Tang, X.,
1026 and Morlighem, M.: Basal friction of Fleming Glacier, Antarctica—PartGuo, X.: Where is the
1027 1: Sensitivity of inversion to temperature and bedrock uncertainty, million-year-old ice at
1028 Dome A?, The Cryosphere, 12, 2637–26521651–1663, <https://doi.org/10.5194/tc-12-2637-2018>, 2018a2018.

1029 Zhao, L., Moore, J. C., Sun, B., Tang, X., and Guo, X.: Where is the 1 million year old ice at Dome
1030 A?, The Cryosphere, 12, 1651–1663, <https://doi.org/10.5194/tc-12-1651-2018>, 2018b.

1031 Zhang, X., Dong, X., Zeng, J., Hou, S., Smeets, P., Reijmer, C. H., and Wang, Y., Spatiotemporal
1032 Reconstruction of Antarctic Near-Surface Air Temperature from MODIS Observations, J.
1033 Clim., 35, 5537–5553, 2022.

1034 Zwinger, T., Schäfer, M., Martín, C., and Moore, J. C.: Influence of anisotropy on velocity and age
1035 distribution at Scharffenbergbotnen blue ice area, The Cryosphere, 8, 607–621,
1036 <https://doi.org/10.5194/tc-8-607-2014>, 2014.

1037

1038